Resource

Molecular Cell

HMGB2 Loss upon Senescence Entry Disrupts Genomic Organization and Induces CTCF Clustering across Cell Types

Graphical Abstract

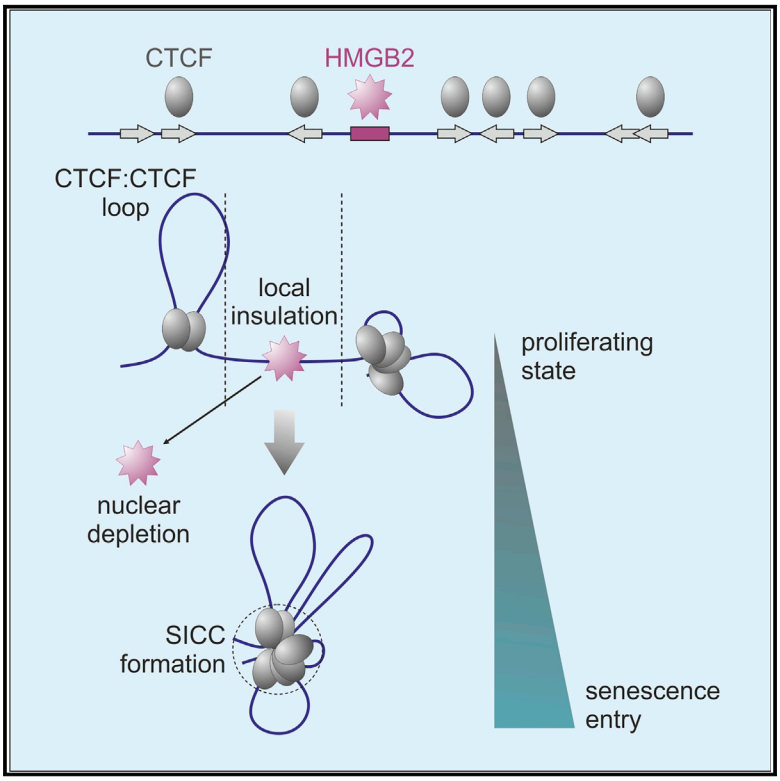

Authors

Anne Zirkel, Milos Nikolic, Konstantinos Sofiadis, ..., Davide Marenduzzo, Karsten Rippe, Argyris Papantonis

Correspondence

argyris.papantonis@uni-koeln.de

In Brief

Zirkel et al. use three distinct primary human cell types to show that nuclear depletion of HMGB2 constitutes an early event on the path to replicative senescence controlling heterochromatic and transcriptional remodeling. HMGB2 binds chromatin at TAD boundaries and forms loops, and its loss is instructive for senescence-induced CTCF spatial clustering.

Highlights

- HMGB2 nuclear depletion is an early event on the path to senescence
- HMGB2 binds positions both at TAD boundaries and within TADs
- The loss of HMGB2 induces heterochromatic and transcriptional changes
- HMGB2 suffices for instructing and rescuing senescence-induced CTCF clustering

Zirkel et al., 2018, Molecular Cell *70*, 1–15
May 17, 2018
https://doi.org/10.1016/j.molcel.2018.03.030

CellPress

Please cite this article in press as: Zirkel et al., HMGB2 Loss upon Senescence Entry Disrupts Genomic Organization and Induces CTCF Clustering across Cell Types, Molecular Cell (2018), https://doi.org/10.1016/j.molcel.2018.03.030

Molecular Cell
Resource

HMGB2 Loss upon Senescence Entry Disrupts Genomic Organization and Induces CTCF Clustering across Cell Types

Anne Zirkel,[1,10] Milos Nikolic,[1,10] Konstantinos Sofiadis,[1,10] Jan-Philipp Mallm,[2] Chris A. Brackley,[3] Henrike Gothe,[4] Oliver Drechsel,[4] Christian Becker,[5] Janine Altmüller,[1,5] Natasa Josipovic,[1] Theodore Georgomanolis,[1] Lilija Brant,[1] Julia Franzen,[6] Mirjam Koker,[7] Eduardo G. Gusmao,[1,8] Ivan G. Costa,[8] Roland T. Ullrich,[1,7] Wolfgang Wagner,[6] Vassilis Roukos,[4] Peter Nürnberg,[1,5,9] Davide Marenduzzo,[3] Karsten Rippe,[2] and Argyris Papantonis[1,11,*]
[1]Center for Molecular Medicine Cologne, University of Cologne, 50931 Cologne, Germany
[2]German Cancer Research Center and Bioquant, 69120 Heidelberg, Germany
[3]School of Physics and Astronomy, University of Edinburgh, EH9 3FD Edinburgh, UK
[4]Institute of Molecular Biology, 55128 Mainz, Germany
[5]Cologne Center for Genomics, University of Cologne, 50931 Cologne, Germany
[6]Helmholtz Institute for Biomedical Engineering, RWTH Aachen University Medical School, 52074 Aachen, Germany
[7]Clinic I of Internal Medicine and Center for Integrated Oncology, University Hospital Cologne, 50931 Cologne, Germany
[8]Interdisciplinary Centre for Clinical Research, RWTH Aachen University Medical School, 52062 Aachen, Germany
[9]Cologne Excellence Cluster on Cellular Stress Responses in Aging-Associated Diseases (CECAD), University of Cologne, 50931 Cologne, Germany
[10]These authors contributed equally
[11]Lead Contact
*Correspondence: argyris.papantonis@uni-koeln.de
https://doi.org/10.1016/j.molcel.2018.03.030

SUMMARY

Processes like cellular senescence are characterized by complex events giving rise to heterogeneous cell populations. However, the early molecular events driving this cascade remain elusive. We hypothesized that senescence entry is triggered by an early disruption of the cells' three-dimensional (3D) genome organization. To test this, we combined Hi-C, single-cell and population transcriptomics, imaging, and *in silico* modeling of three distinct cells types entering senescence. Genes involved in DNA conformation maintenance are suppressed upon senescence entry across all cell types. We show that nuclear depletion of the abundant HMGB2 protein occurs early on the path to senescence and coincides with the dramatic spatial clustering of CTCF. Knocking down *HMGB2* suffices for senescence-induced CTCF clustering and for loop reshuffling, while ectopically expressing *HMGB2* rescues these effects. Our data suggest that HMGB2-mediated genomic reorganization constitutes a primer for the ensuing senescent program.

INTRODUCTION

Since the original description of *in vitro* replicative senescence (Hayflick, 1965), *in vivo* implications in development, wound healing, organismal aging, and disease have been uncovered (van Deursen, 2014). In addition, clearance of senescent cells in mice was shown to improve health- and lifespan (de Keizer, 2017). Senescence entry is a result of integrated autocrine and paracrine signaling in the population (Acosta et al., 2013; Davalos et al., 2013; Hoare and Narita, 2017) triggering replicative arrest, gene expression changes, secretory activity, and chromatin reorganization (Rai and Adams, 2013). Telomere shortening (Herbig et al., 2004), reorganization of heterochromatin and the lamina (Narita et al., 2006; Sadaie et al., 2013; Shah et al., 2013; Swanson et al., 2013; Zhang et al., 2005), activation of transposable elements (De Cecco et al., 2013), or epigenetic changes on histones and the primary DNA sequence have been observed (Cruickshanks et al., 2013; Franzen et al., 2017; Neyret-Kahn et al., 2013). Still, despite some of these events sufficing for replicative arrest, early events signaling senescence entry remain elusive.

Thus, senescence is an attractive model for studying the structure-to-function relationship of chromosomes. This is now feasible due to the advent of Hi-C technology that captures spatial interactions within and between chromosomes (Belton et al., 2012). As a result of Hi-C studies, we now understand that chromosomes are partitioned into active A and inactive B compartments at the Mbp scale, and into consecutive topologically associating domains (TADs) at the sub-Mbp scale. TADs harbor chromatin loops that tend to interact with one another more frequently than with loops in other TADs (Dixon et al., 2012). This higher-order organization is tightly linked to gene expression regulation, but also to cell-cycle progression (Naumova et al., 2013).

For senescence, Hi-C has only been applied to fibroblasts undergoing oncogene-induced senescence (OIS) or maintained long term in "deep" senescence, both constituting end-point states. In OIS, interaction loss within heterochromatin and

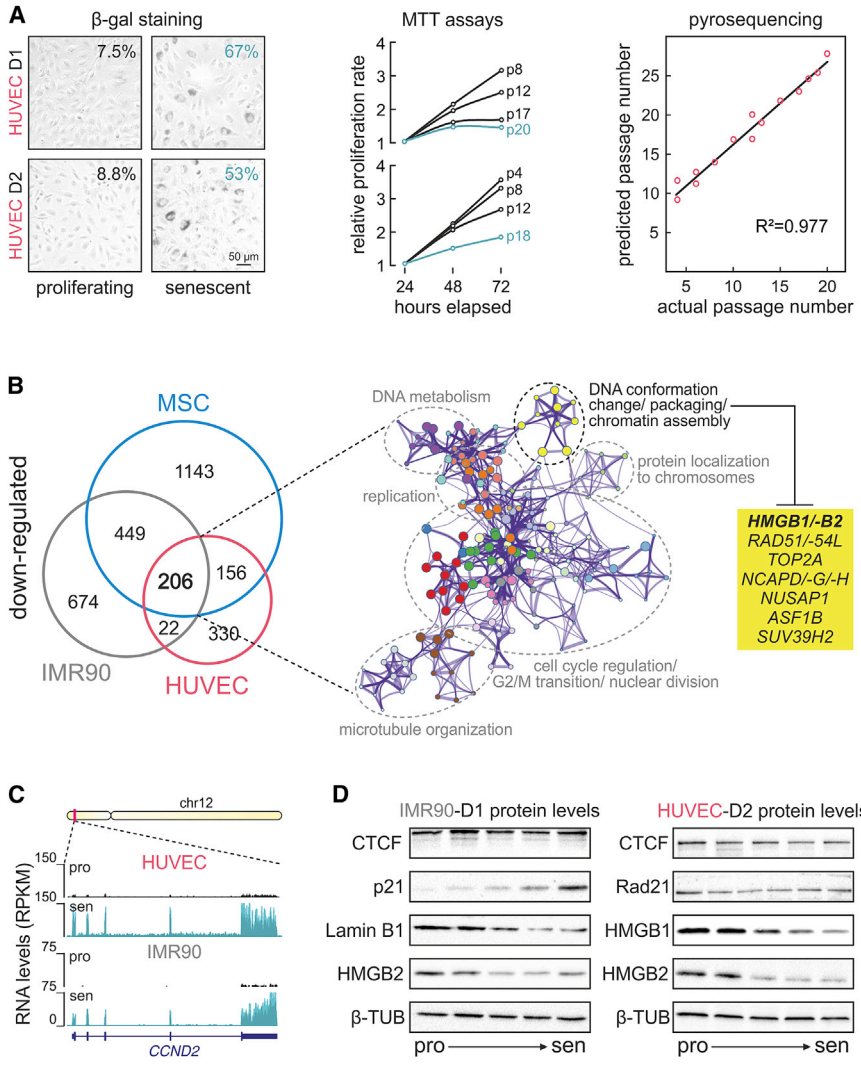

Figure 1. Senescence Entry Signals Suppression of Specific Pathways

(A) Left: β-galactosidase (β-gal) staining of proliferating and senescent HUVEC donors D1 and D2; percent of β-gal-positive cells is indicated. Middle: MTT assays for D1 and D2 at different passages; cells were deemed senescent at passage 20 and 18, respectively (green lines). Right: Spearman's correlation (R^2) between actual and predicted HUVEC passage based on the methylation at six CpGs.

(B) Left: genes downregulated in senescence across cell types. Right: pathways associated with shared downregulated genes. Nodes (yellow) containing genes involved in DNA conformation, DNA packaging, or chromatin assembly are highlighted, and selected genes are listed (box).

(C) *CCND2* locus RNA-seq profiles in HUVECs and IMR90s.

(D) HMGB1, HMGB2, CTCF, Lamin B1, Rad21, and p21 western blots at five different passages in HUVECs and IMR90s; β-tubulin provides a control.

lamin-associated regions was observed, and in a next step clustering of heterochromatic stretches to form senescence-associated heterochromatic foci (SAHFs; Chandra et al., 2015). In "deep" senescence, shorter-range interactions are favored over longer-range ones, thus compacting chromosome arms, while centromeres decondense (Criscione et al., 2016). Therefore, whether spatial genome reorganization triggers replicative senescence entry remains unaddressed.

We used three human primary cell types from individual donors—umbilical vein endothelial cells (HUVECs), fetal lung fibroblasts (IMR90s), and mesenchymal stromal cells (MSCs)—to identify a shared regulatory backbone instructing replicative arrest. We combined genomics, super-resolution microscopy, and single-cell sequencing to discover that proteins of the high-mobility group B (HMGB) family are implicated in regulating specific TAD boundaries, as well as in the spatial clustering of CTCF-bound chromatin. HMGBs are abundant nuclear proteins with characteristic HMG-box DNA-binding domains; they are known to distort DNA via unwinding, bending, or looping (Stros, 2010). This renders them important for transcription, nucleosome remodeling, genome integrity, and recombination (Bonaldi et al., 2002; Laurent et al., 2010; Redmond et al., 2015; Lee et al., 2010; Little et al., 2013; Polanská et al., 2012). Critically, HMGBs are depleted from cell nuclei in senescent and aging tissues (Abraham et al., 2013; Aird et al., 2016; Davalos et al., 2013; Ly et al., 2000; Taniguchi et al., 2009), and markedly overexpressed across cancer types (http://www.cbioportal.org/). Despite their physiological relevance, the binding and roles of HMGBs on chromatin remain enigmatic, but this work sheds new light onto their connection to the proliferative capacity, 3D genome folding, and transcriptional output of primary cells.

RESULTS

A Shared Regulatory Backbone for Senescence Entry across Cell Types

We hypothesized that different lineages share a common regulatory backbone controlling entry into replicative senescence. To test this, we obtained three distinct primary human cell types from individual donors/isolations: HUVECs (mesodermal) from three single donors, two isolates of IMR90s (endodermal), and MSCs (multipotent) from five donors. As the path to senescence is characterized by heterogeneity (Smith and Whitney, 1980), we used phenotypic and molecular markers to define the passage at which ~65% of cells in each population had entered senescence. Cells staining positive for β-galactosidase, showing significantly reduced proliferation, and specific methylation changes at six senescence-predictive CpGs (Franzen et al., 2017) were deemed senescent (Figures 1A, S1A, and S1B).

Note here that one HUVEC and one MSC donor displayed a limited number of population doublings until senescence and, despite their convergent gene expression profiles, were excluded from further analyses. This highlights the idiosyncratic nature of cellular aging due to donor-specific features.

Total RNA from proliferating and senescent populations from all cell types and donors was collected, depleted of rRNA, poly(A)$^+$-enriched (except for HUVECs), and sequenced to >50 million read pairs each. Following mapping to the genome (hg19), read counts were normalized *in silico* to control for differences in transcript abundance as a result of senescence entry (Risso et al., 2014; Figure S1C). Differential gene expression analysis revealed different numbers of up- and downregulated genes in each cell type (±0.6 $\log_2$ fold change), which nonetheless showed converging gene ontology (GO) profiles (Figures S1D and S1E). A total of 153 upregulated genes, mostly involved in cell growth, p53 responses, and ECM reorganization, were shared by all cell types (Figure S1F). On the other hand, the 206 shared downregulated genes were associated with cell-cycle regulation, replication, and DNA metabolism, but critically also with DNA conformation, chromatin organization, and DNA packaging (Figure 1B). The latter terms are due to genes like *HMGB1/B2*, *TOP2A*, *NCAPD/-G/-H*, or *ASF1*, and aligned with our hypothesis on 3D chromatin reorganization upon senescence entry.

We validated gene expression changes by comparison to available data from senescent s (Rai et al., 2014; Figure S1G), and by time course qRT-PCR on selected targets (Figure S1H). We also isolated and analyzed nascent RNA from proliferative/senescent IMR90s via "factory" RNA sequencing (RNA-seq) (Melnik et al., 2016) to show that most regulation occurs at the level of transcription (Figures 1C and S1I). Due to their ability to bend DNA *in vitro*, their reduced expression in senescent and aging tissue *in vivo*, and their unknown roles on chromatin, we focused on HMGB1/B2 and verified their suppression at the protein level in both IMR90s and HUVECs (Figure 1D).

Single-Cell mRNA Profiling of Senescence Entry Cells

Transcriptional heterogeneity is inherent to senescent cell populations (Hernandez-Segura et al., 2017). To show that *HMGB1/B2* are suppressed before known senescence markers appear, we performed single-cell mRNA sequencing (scRNA-seq) by analyzing ~8,300 proliferating and ~5,200 senescent HUVECs on a 10X Genomics platform. Following multiplexed sequencing, we generated ~30,000 reads per cell in either state, and >2,500 individual transcripts were robustly captured per cell. Next, we clustered cells from each state based on their individual expression profiles. Unsupervised clustering showed proliferating and senescent cells segregating into four clusters (Figure 2A). Interestingly, the three major senescent cell clusters reflected the relative distributions of *HMGB2* and *CDKN1A* (p21) expression: low *HMGB2* levels mostly marked cells with medium-to-high *CDKN1A* levels (i.e., replicatively arrested cells), yet >1,800 cells carried little *HMGB2* mRNA without *CDKN1A* induction. Similarly, >2,500 proliferating cells showed robust *HMGB1* but already low *HMGB2* levels (Figures 2B and 2C). Senescent cells lacking *HMGB2* expression were also marked by high levels of the *IL6* and *IL8* SASP genes (Figure 2B). Importantly, the gene expression profiles previously reported to hold key roles in senescence and the cell cycle, like *LMNB1*, *EZH2*, *PCNA*, or *CCNA2*, also differentially marked proliferating and senescent subpopulations, but were less informative for clustering (Figure 2B).

Last, we exploited the heterogeneity in HUVEC populations to perform pseudo-time course analyses of scRNA-seq data (Haghverdi et al., 2016). We found that the gradual drop in *HMGB1/B2* levels in proliferating HUVECs sufficed for describing seven states that appear consecutively derived from one another (Figure 2D). On the other hand, the eight senescent cell states along the main path display variable amounts of *HMGB1/B2* and are best described by a rise in *CDKN1A* levels and by strong *IL8* and *CXCL1* SASP gene expression. Still, subclusters 1 and 4 had *HMGB2* suppressed, but *HMGB1* robustly detected (Figure 2D). This, to our knowledge, first ever transcriptome of single replicatively senescent cells documents how *HMGB2* suppression is an early event marking senescence entry.

HMGB2 Depletion Precedes p21 Activation and Induces Heterochromatic Changes

To complement scRNA-seq data and examine changes in HMGB1/B2 titers, we turned to single-cell immunofluorescence. Super-resolution imaging found the abundant HMGB1/B2 proteins localizing in non-DAPI-dense nuclear areas (Figure S2A). Widefield microscopy coupled to semi-automated quantification of fluorescence levels (STAR Methods) revealed that senescent nuclei almost doubled in area across cell types, and larger nuclei were almost invariably β-galactosidase positive (Figures 3A and 3B). This urged us to stratify all microscopy data according to increasing nuclear sizes. This way we could verify that HMGB1/B2 were depleted from essentially all large HUVEC, IMR90, or MSC nuclei (Figure 3C). Although HMGB1/B2 nuclear depletion appeared coordinated among individual cells ($\rho = 0.81$), p21 upregulation—a hallmark of replicative arrest—correlated rather poorly with low HMGB2 titers ($\rho = 0.35$; Figures 3D and 3E). This agrees with our scRNA-seq data in which HUVECs with low *HMGB2* titers and no *CDKN1A* and/or robust *HMGB1* levels represent an early state on the path to senescence.

Focusing on size-discretized nuclei, we found that larger and HMGB2-depleted nuclei show specific decrease in H3K27me3 levels, the mark characteristic of facultative heterochromatin (Shah et al., 2013), while also displaying increased HP1α levels (marking constitutive heterochromatin, but without SAHF formation as in OIS; Narita et al., 2006; Figure S2B). This was concomitant with a drop in histone acetylation measured using H3K27ac or H4K16ac as markers (Figures S2C and S2D). Finally, increased H3K9 methylation was confirmed in senescent HUVECs and IMR90s via ELISA (Figure S2E), while the senescent-induced drop in H3K27ac/me3 was in line with changes in H3K27ac/me3 chromatin immunoprecipitation sequencing (ChIP-seq) signal (Figures S2F and S2G).

Senescence Entry Is Marked by Changes in 3D Chromatin Folding

Population and single-cell data encouraged us to interrogate changes in whole-genome 3D folding upon senescence entry

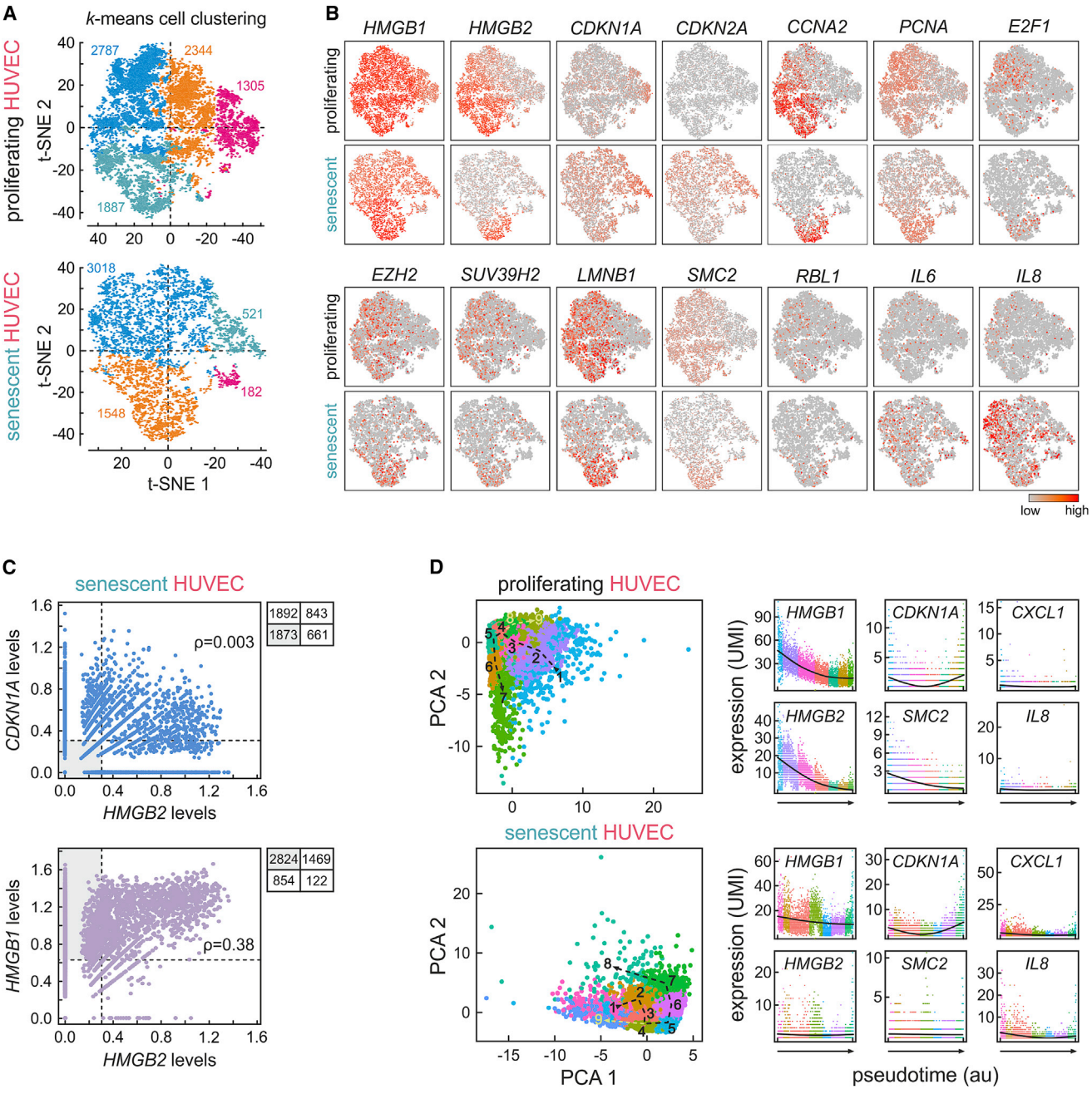

Figure 2. scRNA-Seq Highlights Early *HMGB2* Suppression

(A) Unsupervised clustering of scRNA-seq data from proliferating or senescent HUVECs. Each dot represents one cell, and number of cells per cluster is indicated.

(B) mRNA levels of 14 senescence-regulated genes in proliferating or senescent cells.

(C) *HMGB2* scRNA-seq read counts were plotted against *HMGB1* and *CDKN1A* read counts; median values minus one SD (dotted lines), Pearson's correlation coefficients (ρ), and the number of cells in each quadrant are indicated.

(D) Left: pseudo-time course clustering of scRNA-seq data from proliferating or senescent HUVECs. The main path (black line) also breaks into a secondary leg (yellow line). Right: expression of six key genes in the clusters along the main path of proliferating (top) or senescent cells (bottom).

via Hi-C. We used *Hind*III and obtained >300 million read pairs per donor and condition, after sequencing two technical replicates from two HUVEC and IMR90 donors/isolates and one MSC donor (Figure S3A). After confirming reproducibility between Hi-C maps from the same cell type and condition (Figure S3B), we merged replicates and could now afford ~20-kbp resolution of spatial chromatin interactions in both proliferating and senescent cells (higher than that afforded for "deep"

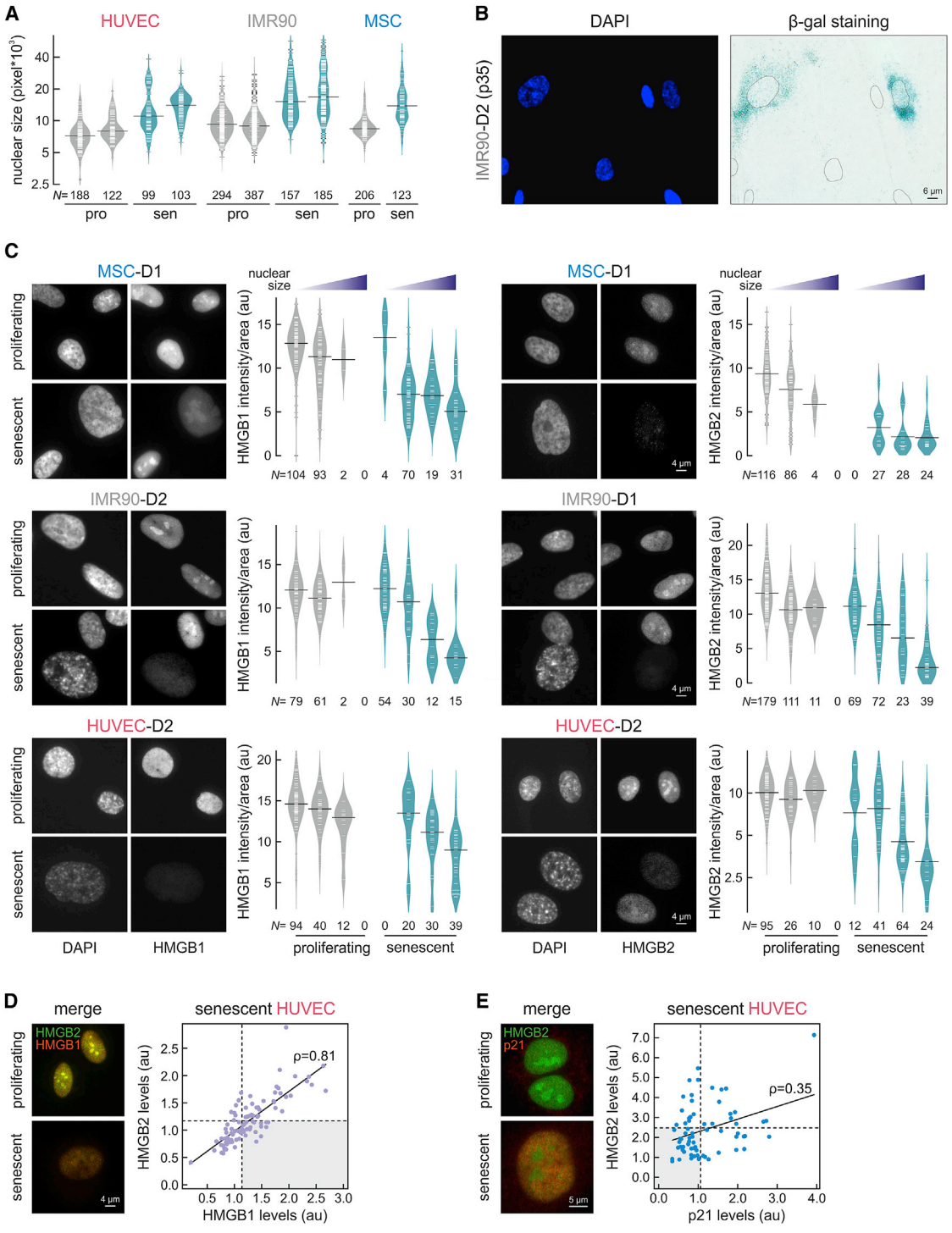

Figure 3. Senescence Entry Is Characterized by HMGB2 Nuclear Loss

(A) Distribution of nuclear sizes in proliferating (gray) or senescent (green) HUVECs, IMR90s, and MSCs. The total number of nuclei measured (N) is indicated.

(B) Typical images of senescent IMR90 stained for β-galactosidase and DAPI.

(C) Typical images of proliferating/senescent MSCs, IMR90s, and HUVECs immunostained for HMGB1/B2 (left). Bean plots (right) show changes in HMGB1/B2 levels in cells grouped according to increasing nuclear size. The total number of nuclei measured (N) is indicated.

(D) Typical images of proliferating/senescent HUVECs immunostained for HMGB1/B2. Fluorescence levels were used to produce scatterplots; median values minus one SD (dashed lines) and Pearson's correlation coefficients (ρ) are indicated.

(E) As in (D), but for HMGB2 and p21.

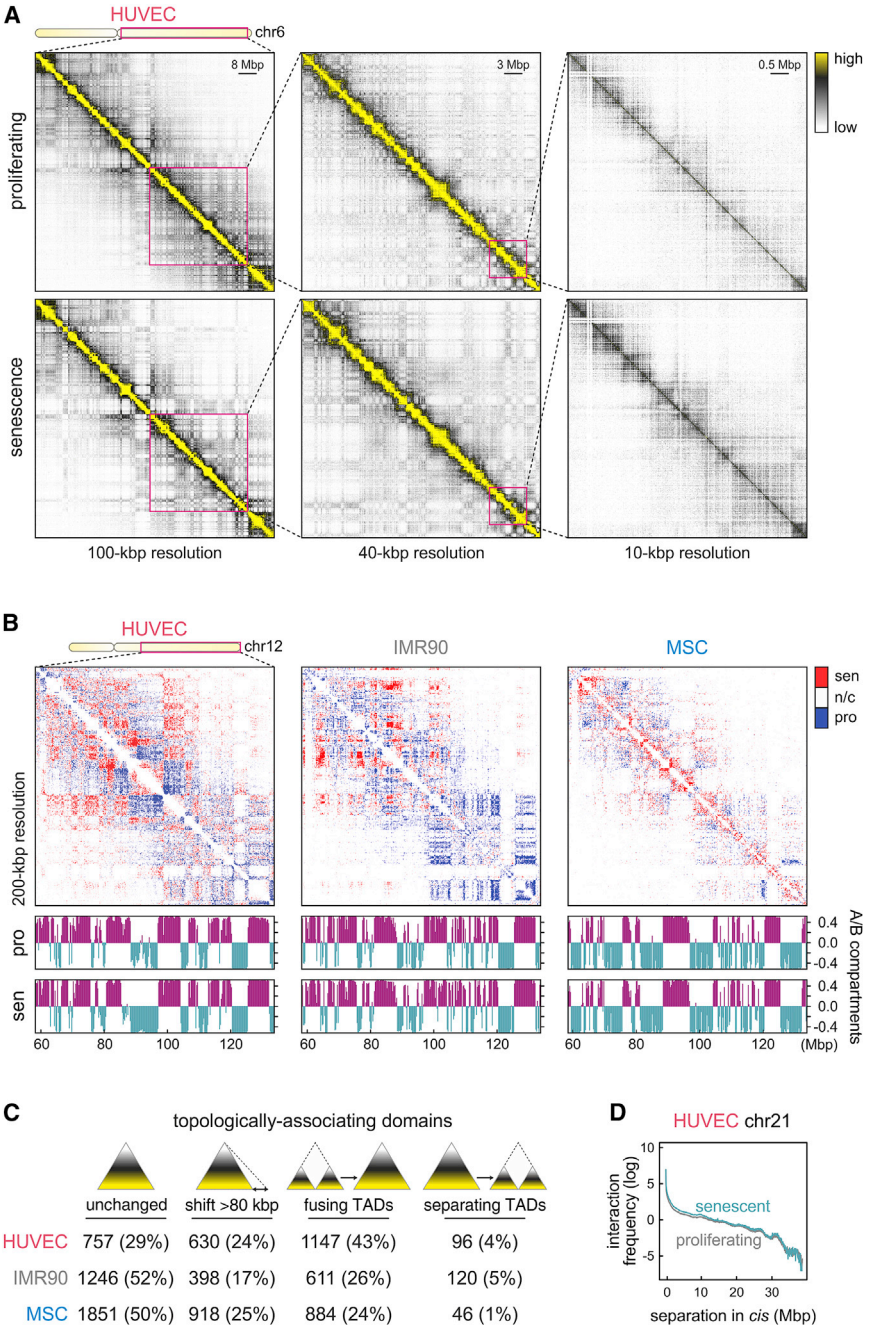

Figure 4. Senescence Entry Is Accompanied by 3D Genome Reorganization

(A) Hi-C contact frequencies along the long arm of chr6 from proliferating and senescent HUVECs at increasing resolution.

(B) Binary increase/decrease in Hi-C contact frequencies between senescent and proliferating HUVECs, IMR90s, or MSCs along a subregion of chr12. Aligned below are graphs showing A (purple) and B compartments (green) for each cell type and condition.

(C) The number of TADs (percentages in brackets) that remain unchanged, shift one boundary, fuse into one larger TAD, or separate into smaller TADs upon senescence is listed for all cell types.

(D) Interaction frequency decay as a function of *cis*-separation between fragments for chr21 in proliferating or senescent HUVEC Hi-C data.

senescence; Criscione et al., 2016). Initially, we looked into interchromosomal interaction changes between whole chromosomes upon senescence entry; both HUVEC and IMR90 chromosomes mostly displayed decreased, cell-type-specific *trans*-interactions (Figure S3C).

We next examined intrachromosomal interactions. Two features stand out when comparing Hi-C interaction maps from proliferating and senescent HUVECs: first, stronger longer-range interactions emerge upon senescence entry; second, apparent insulation, especially between large higher-order domains, is seen in senescent cells (Figures 4A and S4A). This holds true across all cell types and chromosomes studied (Figures S3D and S4A–S4C). Interaction changes between single donors/isolates visualized at a 200 kbp resolution are almost invariably of the same nature (Figure S3E). But when different cell types are compared, the same chromosomal regions refold in a cell-type-specific manner upon senescence (Figures 4B and S4F), and this is in line with senescence epigenetically reprogramming each cell type.

In addition, most Hi-C data to date display more changes at the level of A/B compartments than at that of TADs (e.g., Criscione et al., 2016; Dixon et al., 2012). However, we observed limited switching between A/B compartments (Figures 4B and S5A). We went on to define TADs in our Hi-C data from both conditions across cell types. We employed "TADtool" (Kruse et al., 2016) and the resolution afforded by our lowest-covered dataset (40-kbp resolution in MSCs), while applying similar TAD-calling parameters for proliferating or senescent data in each cell type. This analysis returned a total of ~3,000 TADs for HUVECs and IMR90s and ~3,500 for MSCs in either state. In IMR90s and MSCs, ~50% of TADs remain unchanged upon senescence entry, while ~20% shift at least one of their boundaries by ≥80 kbp and ~25% fuse into larger TADs (Figure 4C). TAD changes were more drastic in HUVECs, with 24% TADs shifting boundaries and 43% fusing into larger ones—in agreement with the strong differences seen in HUVEC Hi-C (Figures S4A–S4C). Interaction decay plots revealed widespread changes in both longer- and shorter-range interactions upon senescence entry (Figures 4D and S5B), which differs from what was observed for "deep" senescence (Criscione et al., 2016; Figures S5C and S5D).

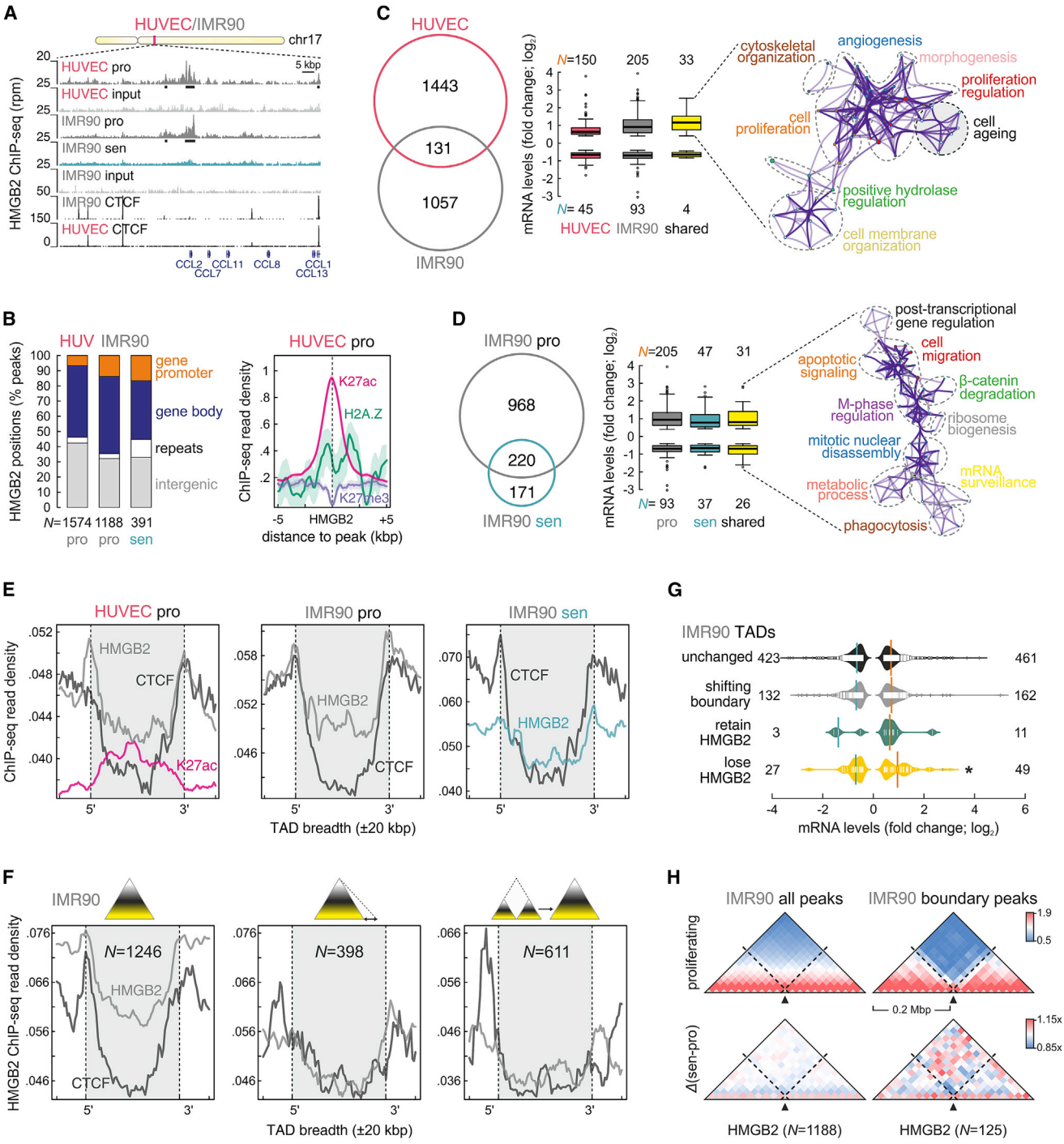

Figure 5. HMGB2 Chromatin-Binding Properties

(A) HMGB2 ChIP-seq from proliferating/senescent HUVECs and IMR90s along a chr17 locus; CTCF ChIP-seq and input profiles are aligned below.

(B) Left: percentage of HMGB2 peaks from proliferating/senescent HUVECs and IMR90s overlapping promoters, gene bodies, repeats, or intergenic space. The total number of peaks (N) per dataset is indicated. Right: distribution of H3K27ac, H3K27me3, and H2A.Z ChIP-seq signal in the 10 kbp around HUVEC HMGB2 peaks.

(C) Left: HMGB2 peaks shared between HUVECs and IMR90s. Middle: $\log_2$ fold changes of differentially expressed genes bound by HMGB2. The total number of genes (N) is indicated. Right: GO terms associated with HMGB2-bound upregulated genes in both HUVECs and IMR90s.

(D) As in (C), but for HMGB2 peaks shared between proliferating and senescent IMR90s.

(E) Distribution of HMGB2 ChIP-seq signal along TADs (±20 kbp) in proliferating/senescent HUVECs or IMR90s; CTCF and H3K27ac distributions serve as controls.

(legend continued on next page)

Finally, we used 3D DNA-fluorescence *in situ* hybridization (FISH) (Roukos et al., 2015), with probes targeting three increasingly separated regions on the long arm of chr12 to query conformational changes. In senescent HUVECs, which are predominantly tetraploid (Figure S6A), FISH showed all probes becoming more separated from one another upon senescence and assuming less peripheral positioning in the larger senescent nuclei (Figures S6B–S6E). In IMR90s, which remain diploid, the two most distant probes come significantly closer together upon senescence, while the intervening one separates out, and only one probe pair shows less peripheral positioning (Figures S9A–S9E). Critically, in both HUVECs and IMR90s the FISH data agree with changes seen by Hi-C (i.e., increased probe separation matched by decreased interaction frequency; Figures S6C and S6E).

Heterochromatic Remodeling Does Not Adequately Explain 3D Genome Reorganization

Genome reorganization in OIS and in "deep" senescence involves formation of characteristic SAHFs (Chandra et al., 2015) and strong chromatin compaction, respectively (Criscione et al., 2016). Here, senescence entry coincides with a heterochromatic shift (Figure S2B), and we asked whether this suffices to explain the changes seen by Hi-C (Figure S4). As it is not straightforward to experimentally decouple HMGB1/B2 loss from heterochromatic changes, we used molecular dynamics simulations of 3D chromatin folding. This *in silico* approach models preferential low-attraction interactions of loci on the basis of their chromatin identity (defined using ENCODE ChIP-seq; STAR Methods) that faithfully recapitulate Hi-C interactions (Brackley et al., 2016a). We focused on a 15-Mbp region on the long arm of chr12. Based on our ChIP-seq data, heterochromatic positions were kept the same for both states modeled, but H3K9me3-mediated interaction strength was increased by ~30% in the senescent model (consistent with Figures S2B–S2G). Following multiple iterations, average interaction profiles only partly recapitulated experimental Hi-C profiles (Figures S6F and S6G). Thus, as this strengthened heterochromatic bridging did not sufficiently explain all changes occurring upon senescence entry (Figure S6H), we went on to explore a potential contribution of HMGB1/B2 in chromatin folding.

HMGB1 and HMGB2 Bind Non-overlapping Active Chromatin Sites

Our understanding of the roles of HMGB1/B2 remains incomplete due to the fact that formaldehyde crosslinking fails to capture HMG box factors bound to chromatin (Pallier et al., 2003; Redmond et al., 2015; Teves et al., 2016). To circumvent this, we devised a dual-crosslinking approach for HMGB1/B2 ChIP-seq (STAR Methods) and identified 1,574 and 1,188 robust HMGB2 peaks in proliferating HUVECs and IMR90s, respectively; we also identified 391 peaks in senescent IMR90s (Figures 5A and S7A). HMGB2 mostly binds promoters or bodies of active genes associated with processes relevant to senescence (e.g., ECM organization, wound healing, or mitotic phase transition; Figures 5B and S7B). Notably, at least twice as many genes bound by HMGB2 are up- rather than downregulated (Figure 5C). As HUVECs and IMR90s deploy different gene expression programs and HMGB2 predominantly associates with active loci, the two cell types only share 131 (~10%) HMGB2 peaks. Still, there are 8-fold more up- than downregulated genes associated with these 131 peaks, and they are linked to such processes as cell proliferation and cell aging (Figure 5C).

Of the 391 HMGB2 peaks found in the senescent IMR90 population, 220 were at positions also bound in proliferative cells (and are thus the result of heterogeneity rather than of persistent binding), whereas 171 seem to form *de novo*. These 220 peaks are associated with mitotic processes and mRNA surveillance (Figure 5D). Critically, none of the 171 senescence-specific peaks overlapped SASP genes as was proposed for OIS (Aird et al., 2016; Figure S7D). Thus, remodeling of HMGB2 binding in replicative senescence does not involve SASP loci.

Next, to identify transcription factors (TFs) potentially co-bound with HMGB2, we analyzed DNase I-hypersensitive footprints under HMGB2 ChIP-seq peaks for known TF motif enrichment. Following filtering for well-expressed TFs, this analysis returned a number of candidate TFs that included architectural ones, like CTCF; those relevant to cell-cycle regulation, like E2F-family members and FOXP1/2; or those involved in proinflammatory signaling, like NFKB2 and RELA (Figure S7E). These motifs are enriched under HMGB2 peaks from proliferative cells, which implies that loss of HMGB1/B2 from these positions might either dismantle co-bound complexes (e.g., in the case of E2F factors to hinder cell-cycle progression) or facilitate assembly of new ones (e.g., in the case of proinflammatory SASP-related TFs that remain largely inactive in proliferating cells).

Finally, using the same dual-crosslinking approach, we generated HMGB1 ChIP-seq profiles in proliferating HUVECs and IMR90s. We identified 810 and 593 HMGB1 peaks, respectively, more than 30% of which were intergenic and rarely overlapped HMGB2-bound sites, suggesting that the two factors have non-overlapping functions (Figures S7F and S7G).

Chromatin-Bound HMGB2 Marks a Subset of TAD Boundaries

Using high-resolution Hi-C data from IMR90s (Rao et al., 2014), we found that HMGB2 ChIP-seq peaks display good correlation to positions of interaction insulation (i.e., at TAD/sub-TAD boundaries; Figure S8A). Correlation of HMGB2 peaks to TAD extremities from proliferating HUVECs and IMR90s showed that they mark TAD boundaries comparably to CTCF, and this demarcation markedly weakened for TADs from senescent cells

(F) As in (E), but for IMR90 TADs that do not change (left), shift one boundary (middle), or fuse into one larger TAD (right). The total number of TADs in each group (N) is indicated.

(G) Log_2 fold changes of differentially expressed genes located within the different TAD subsets. The total number of genes in each group (N) is indicated. *Significantly different from "unchanged"; $p < 0.01$, Wilcoxon-Mann-Whitney test.

(H) Normalized Hi-C interaction frequencies (top) or senescence-induced changes Hi-C interactions (bottom) in the 0.4 Mbp around all or TAD-boundary HMGB2 peaks from IMR90s.

(Figure 5E). This implies that TAD boundary changes upon senescence entry (Figure 4F) are linked to HMGB2 depletion from nuclei. In more detail, HMGB2 marks TADs of proliferating cells that both shift their boundaries or remain unchanged in senescence, but not of those that fuse. Intriguingly, non-changing TADs have both boundaries marked by HMGB2, whereas those that shift a boundary display reciprocal demarcation with HMGB2 enriched on one side and CTCF on the other (Figures 5F and S8B). Also, TADs that lose HMGB2 from their boundaries harbor almost twice as many up- compared to downregulated genes compared to other TAD subgroups, in line with our ChIP-seq data (Figures 5C and 5G). Approximately 10% of HMGB2 peaks fell within 40 kbp of a TAD boundary in proliferating cells, which is significantly more than what would be expected by chance ($p < 0.001$, Fisher's exact test). In order to link HMGB2 boundary positioning to spatial reorganization upon senescence entry, we looked at average Hi-C interaction profiles around HMGB2 peaks. Interaction insulation at HMGB2-bound boundaries collapsed when comparing senescent cells to proliferating cells, and this effect was far less pronounced when considering all peaks (Figure 5H). Of course, since our HUVEC Hi-C afforded higher resolution, we repeated all analyses using 20-kbp resolution data. At this resolution, more TAD changes arose (Figure S8C) and more HMB2 peaks resided at TAD boundaries (~16%; Figure S8D), but demarcation of TAD subgroups, gene expression changes therein, and changes around HMGB2-bound boundaries were still of the same nature (Figures S8E–S8G).

HMGB2 Knockdown Affects Heterochromatin and Induces Spatial CTCF Clustering

The above analyses support a role for HMGB2 in reorganizing chromatin topology upon senescence entry. To functionally establish this, we knocked down *HMGB2* in HUVECs and IMR90s using self-delivering small interfering RNAs (siRNAs) (as primary cells are difficult to transfect and lipofectamine stresses cells and convolutes their phenotypes). This approach strongly depleted the HMGB2 protein (Figure S9A), but unlike previously reported effects for sustained *HMGB1* knockdown (Davalos et al., 2013), the loss of HMGB2 only caused a mild increase in the number of senescent cells in the 72 hr treatment window, while also marginally affecting nuclear size, DNA replication, or gene expression (Figures S9B–S9D). However, after labeling nascent transcripts in live cells via a short (5-min) EUTP pulse and quantifying EU-RNA fluorescence, we uncovered an ~30% drop in nascent RNA levels upon *HMGB2* knockdown; a similar decrease of ~10% in nascent RNA production was seen in senescent IMR90s (Figure 6A). Also, knocking down *HMGB2* sufficed for inducing HP1α and suppressing H3K27me3 levels (Figures 6B and S9E), thus recapitulating the shift between constitutive and facultative heterochromatin seen in senescence. These effects highlight that HMGB2 depletion is an upstream event affecting both the organization of the genome and its functional output.

Next, we asked whether HMGB2 depletion also affected the levels and distribution of CTCF in primary cells. Super-resolution imaging revealed that in proliferating HUVECs, HMGB2 and CTCF foci are tightly alternating and interwoven. Upon senescence entry, CTCF is dramatically reorganized in large senescence-induced CTCF clusters (SICCs) devoid of HMGB2 signal (Figure 6C). SICC formation was consistently found in senescent HUVECs and IMR90s, and *HMGB2* knockdown phenocopied this despite the smaller nuclear sizes in knockdown cells (Figures 6D and S9F–S9H). Notably, SICCs did not overlap HP1α foci (Figure S9I) and thus bear no resemblance to SAHFs and are specific to replicative senescence. SICC formation was not accompanied by strong cohesin reorganization in senescent IMR90s, despite extensive co-localization of CTCF and cohesin on chromatin (Rao et al., 2014). Still, decreased cohesin levels in SICC-positive cells were recorded (Figure S9J). Perhaps surprisingly, <200 HMGB2 peaks from HUVECs or IMR90s were proximal to CTCF peaks, and co-immunoprecipitation of either CTCF or HMGB2 did not reveal physical interaction between the two factors (Figures S9K–S9M). In addition, CTCF binding at both standalone and HMGB2-proximal sites remains unchanged between proliferating and senescent cells (Figure S9N).

To assess the impact of HMGB2 depletion on whole-genome folding, we applied Hi-C to control and *HMGB2* knockdown HUVECs. These data revealed apparent differences between the two states but, just like in senescence, only limited A/B compartment remodeling. At 40-kbp resolution, interactions around HMGB2 peaks were particularly disrupted (Figures 6E and S10A). Changes to TAD boundaries precisely mirrored those seen in senescent HUVECs (Figure 6F) and average interaction profiles around HMGB2- and/or CTCF-bound positions again recapitulated the effects of senescence entry at TAD boundaries (Figures S10B and S10C).

Toward a Molecular Mechanism for SICC Formation

Closer inspection of HMGB2 ChIP-seq aligned to high-resolution HUVEC Hi-C (Rao et al., 2014) revealed loop-like interactions between multiple HMGB2 peaks (Figure 7A). Thus, we inquired whether HMGB2 forms loops similar to CTCF (Rao et al., 2014). We interrogated all pairwise *cis*-interactions involving HMGB2 peaks looking for local Hi-C signal maxima exceeding background. We found ~2,900 and ~5,000 loop structures emanating from HMGB2-bound positions in IMR90s and HUVECs, respectively, with average profiles and intensities that were directly comparable to those of CTCF loops (Figure 7B).

As heterochromatic changes did not fully explain conformation changes observed by Hi-C, we revisited modeling of the 15-Mbp region on chr12. Typically, HMGB2 peaks are positioned between CTCF loops (Figures 7A and 7C) and we hypothesized they might act to insulate further CTCF-CTCF interactions. To model this mode of action, we devised three *in silico* scenarios. First, in proliferating cells, stable looping between convergent CTCF-bound sites was allowed (based on IMR90 loops; Rao et al., 2014), but loops across HMGB2 peaks were disallowed. Second, in "senescence model I," insulation by HMGB2 was alleviated to mimic its depletion from nuclei. Third, in "senescence model II," additional stochastic CTCF-CTCF interactions are favored upon HMGB2 depletion. All three scenarios were implemented on top of the framework used before (Figures S6F–S6H). Each scenario was modeled for 48 iterations and generated increasingly stronger clustering of CTCF-bound chromatin in the absence of HMGB2 (Figures 7C and 7D).

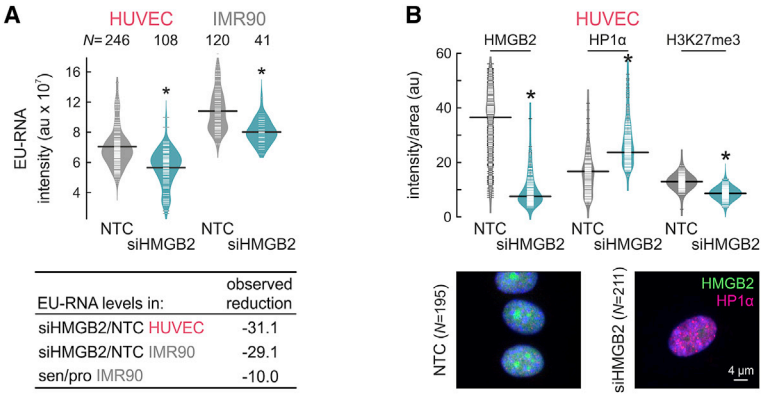

EU-RNA levels in:	observed reduction
siHMGB2/NTC HUVEC	-31.1
siHMGB2/NTC IMR90	-29.1
sen/pro IMR90	-10.0

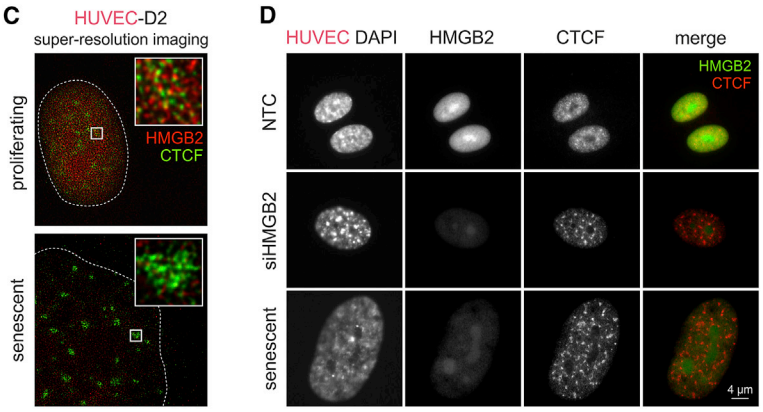

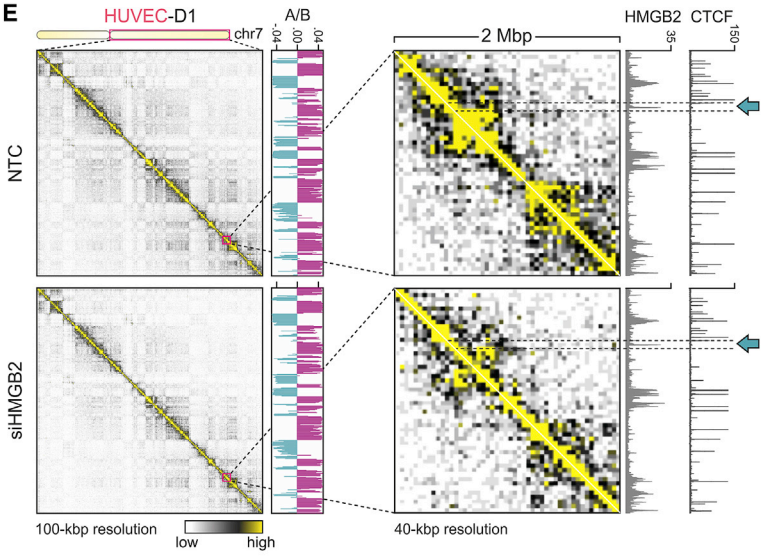

F

HUVEC TADs	unchanged	shift >80 kbp	fusing TADs	separating TADs
senescent vs proliferating	757 (29%)	630 (24%)	1147 (43%)	96 (4%)
siHMGB2 vs NTC	775 (28%)	426 (16%)	1512 (55%)	13 (1%)

Figure 6. *HMGB2* Knockdown Alters CTCF and Chromatin Organization

(A) Decrease in nascent EU-RNA between control (NTC) and knockdown (siHMGB2) HUVECs or IMR90s. *Significantly different from NTC; $p < 0.05$, Wilcoxon-Mann-Whitney test. The total number of cells (N) analyzed is indicated. Average EU-RNA level reduction in knockdown/control is compared (below) to that in senescent/proliferating cells (normalized for the increase in nuclear size).

(B) Concomitant increase in HP1α and decrease in H3K27me3 levels in *HMGB2* knockdown HUVECs. *Significantly different from NTC; $p < 0.05$, Wilcoxon-Mann-Whitney test. Typical images of NTC or siHMGB2 HUVECs immunostained for HMGB2/HP1α (below); the total number of cells (N) analyzed is indicated.

(C) Super-resolution images of proliferating and senescent HUVECs immunostained for HMGB2 and CTCF. Insets: magnified clusters.

(D) Typical widefield images of control, *HMGB2* knockdown, or senescent HUVECs immunostained for HMGB2 and CTCF.

(E) Hi-C contact frequencies along the long arm of chr7 in control and *HMGB2* knockdown HUVECs. One hundred kbp-resolution maps are aligned to A/B compartment plots. Zoom-ins are aligned to HMGB2 and CTCF ChIP-seq and changed interactions around HMGB2 peaks are indicated (arrows).

(F) The number (percentages in brackets) of TADs that remain unchanged, shift one boundary, fuse into one larger TAD, or separate into smaller TADs in senescent/proliferating or *HMGB2* knockdown/control HUVECs.

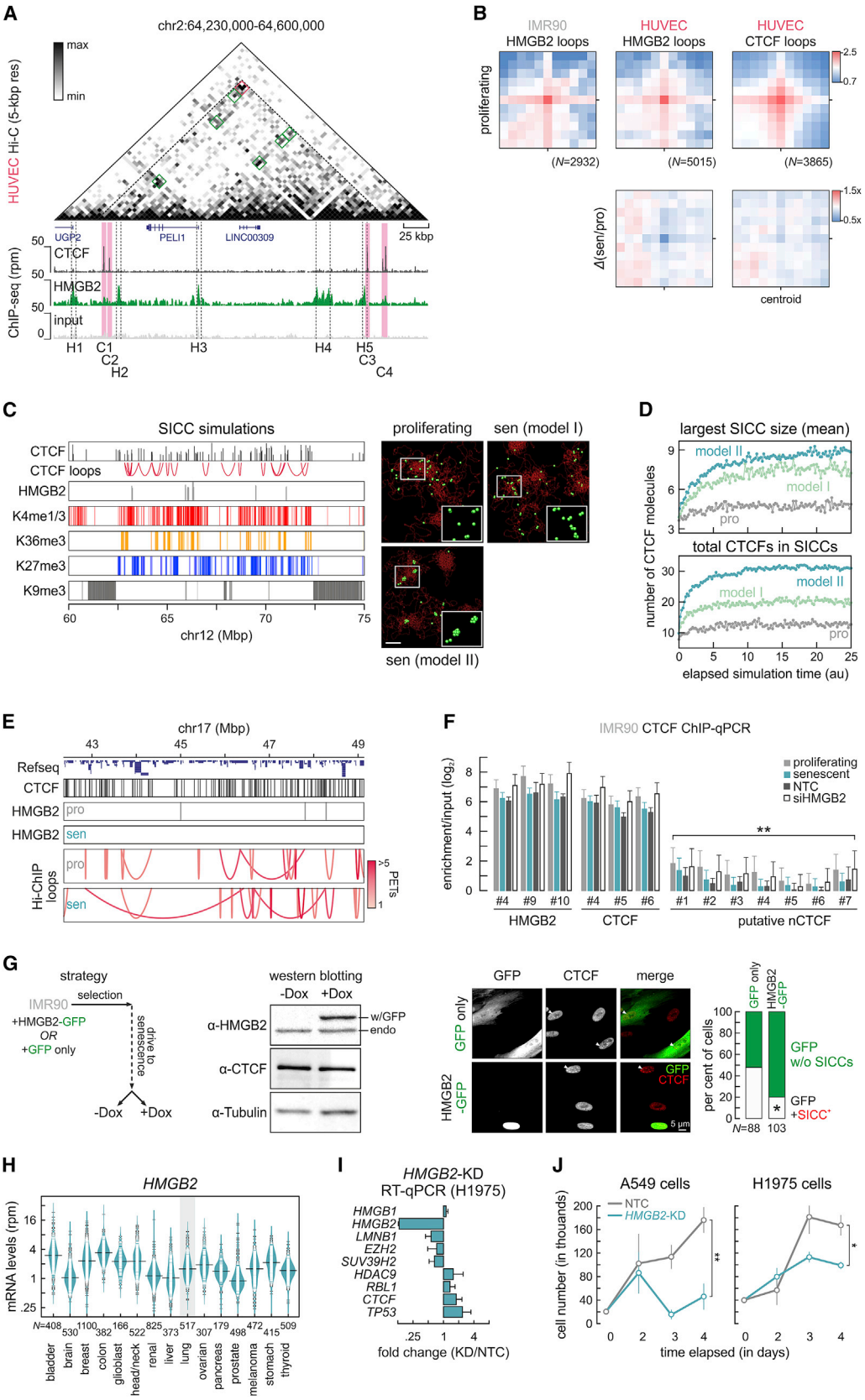

(legend on next page)

To validate these models experimentally, we used HiChIP, which allows spatial interactions owing to a particular TF to be subselected and interrogated independently of all others (Mumbach et al., 2016). We pulled down CTCF and were able to detect ~2,000 and ~1,000 robust CTCF-CTCF loops per condition in HUVECs and IMR90s, respectively (despite lower complexity in CTCF-HiChIP compared to Hi-C libraries; Figure S10D). Comparing intra-chromosomal loops between proliferating and senescent cells revealed increased loop lengths, with ~40% being unique to each state (Figure S10E). Inspection of multi-Mbp genomic stretches populated by CTCF-CTCF loops revealed new long-range CTCF interactions developing around positions where HMGB2 binding is lost, just as our *in silico* models predicted. On the other hand, around positions where HMGB2 binding persists or only occurs in senescence, local loop depletion was observed (Figures 7E and S10F). Hence, HMGB2 peaks indeed function as "insulators" for flanking CTCF-bound sites. However, we ruled out the possibility of CTCF binding at HMGB2 sites that contain motifs resembling those cognate for CTCF by assessing its binding at these "neoCTCF" sites in senescent and *HMGB2* knockdown cells (Figure 7F). Importantly, in both HUVECs and IMR90s, genes within 10 kbp of CTCF loop anchors that reshuffle upon senescence entry display significantly stronger expression changes compared to genes within 10 kbp of static loops (Figure S10G).

Ultimately, to unambiguously link HMGB2 loss to SICC formation, we generated IMR90 populations carrying either a doxycycline-inducible HMGB2-GFP fusion or GFP alone. The constructs were inserted into the genome using a piggybac-based vector. We selected, expanded, and drove cells into senescent heterogeneous populations (to average out clonal variation). *HMGB2* overexpression was induced in senescent cells using doxycycline for 24 hr; ~50% of cells in each population expressed GFP or the HMGB2-GFP fusion (Figure 7G). Of those carrying only GFP, >45% showed strong SICC formation, while significantly fewer (<20%) of those expressing HMGB2-GFP displayed SICCs (Figure 7G). Thus, the nuclear presence or absence of HMGB2 is sufficient and instructive for induction of CTCF clusters upon senescence entry.

Cancer Cell Proliferation Potency Relies on HMGB Factors

HMGB2 proteins are depleted from cell nuclei upon senescence entry and this depletion reduces nascent RNA levels globally (Figure 6A). Conversely, in tumor cells, enhanced proliferative capacity is accompanied by increased global transcription (Kotsantis et al., 2016). Importantly, unlike senescent cells, a large variety of cancer cells display HMGB2 overexpression (Figure 7H). We hypothesized that these higher titers might explain their proliferative potency. As proof of principle, we used two lung lines for *HMGB2* knockdown and could show that suppressing *HMGB2* affects genes like *HDAC9*, *RBL1*, and *TP53* (upregulated), or *LMNB1*, *EZH2*, and *SUV39H2* (downregulated), but not *HMGB1* (Figure 7I). Importantly, this resulted in severe growth arrest of adenocarcinoma cells (Figure 7J), highlighting the potential role of HMGB2 in the maintenance of the proliferative state in cancer.

DISCUSSION

Proliferating cells have mechanisms in place that preserve their inherent chromatin state and its higher-order architecture in conjunction with DNA replication and cell division—and 3D chromatin folding gradually dissolves toward mitosis, before being reinstated after cell division concludes (Naumova et al., 2013). However, how this maintenance is achieved in proliferatively arrested cells remains unclear. Here we hypothesized that entry into senescence of different cell types is governed by a shared regulatory backbone involving an early event of spatial genomic reorganization. We assign this presumed event to the downregulation of genes associated with DNA conformation maintenance, of which *HMGB1/B2* stand out due to their nuclear abundance and inherent ability to bend chromatin (Stros, 2010).

At least 10% of HMGB-bound loci mark TAD boundaries, often coinciding with active gene promoters. This is consistent

Figure 7. HMGB2 Forms Loops and Deters CTCF Clustering

(A) CTCF and HMGB2 ChIP-seq from proliferating HUVECs aligned to high-resolution Hi-C (Rao et al., 2014). Loops (local Hi-C signal maxima) involving CTCF (C1-3; magenta) or HMGB2 peaks (H1-5; green) are demarcated.

(B) Average Hi-C signal in the 100 kbp around CTCF-CTCF loops (separated by ≥150 kbp) from proliferating cells (top) or in senescent versus proliferating cells (bottom).

(C) Left: CTCF peaks and loops, and HMGB2, H3K4me1/3, H3K36me3, H3K27me3, and H3K9me3 ChIP-seq peaks along 15 Mbp of chr12 used in simulations. Right: snapshots of single conformations from proliferating or senescent cell models ("I" and "II") showing chromatin (red) and bound CTCF (green).

(D) Graphs showing increasingly larger SICC sizes (top) and CTCF molecules per SICC (bottom) with simulation time for each of the three models in (C).

(E) HiChIP CTCF loops in a 6.5-Mbp region of chr17 from proliferating and senescent IMR90s. CTCF and HMGB2 peaks in proliferating and senescent IMR90s are aligned above.

(F) Mean ChIP-qPCR enrichment (over input and negative controls; $\log_2 \pm$ SD, n = 2) in different IMR90 populations with primers targeting CTCF, HMGB2, or putative "neoCTCF" sites.

(G) Left: strategy for ectopic HMGB2 expression in IMR90s. Middle: overexpression of endogenous ("endo") or GFP-fusion HMGB2 ("w/GFP"); CTCF and β-tubulin levels provide a control. Right: typical images of Dox-induced IMR90s expressing only GFP or HMGB2-GFP (white arrowheads indicate SICCs), and quantification of GFP-positive cells carrying SICCs (white) with the number of cells in each group (*N*) displayed below. *Significantly different; $p < 0.01$, Fisher's exact test.

(H) *HMGB2* expression levels across 15 cancer types (http://www.cbioportal.org/); the number of patient samples per each type is indicated and lung adenocarcinoma data highlighted.

(I) Changes in selected mRNA levels upon *HMGB2* knockdown in H1975 knockdown versus control cells (mean fold change ± SD; n = 2).

(J) The number of live A549 and H1975 lung adenocarcinoma cells that remain (mean ± SD; n = 3) in the 4 days after *HMGB2* knockdown. *Significantly different mean; $p < 0.01$, unpaired two-tailed Student's t test.

with active protein-coding and tRNA genes overrepresented at TAD boundaries (Dixon et al., 2012) and the notion that transcription acts to partition eukaryotic genomes (Rowley et al., 2017). At HMGB-marked TAD boundaries, the change in activity of the underlying genes coincides with interaction reshuffling upon senescence entry. Notably, HMGB2 contributes to loop formation along human chromosomes, much like CTCF, and this unveils a novel looping factor specifically contributing to 3D genome conformation in proliferating primary cells.

Unlike manipulations of *HMGB1* in fibroblasts (Davalos et al., 2013), *HMGB2* loss does not suffice for senescence induction given the transient nature of a knockdown experiment. However, its suppression recapitulated three key features of senescence entry: it globally reduced transcriptional output, yielding as much as 30% less nascent RNA; it induced a shift between facultative and constitutive heterochromatin; and insulation at HMGB2-bound TAD boundaries collapsed. All three effects were widespread and constitute prime examples of genomic function following form, highlighting how replicative senescence is a suitable and perhaps underappreciated model for studying this relationship in human chromosomes.

Senescent cells are also characterized by the dramatic clustering of CTCF foci into SICCs. In proliferating cells, HMGB2-bound positions seem to insulate flanking CTCF peaks from forming long-range interactions with one another; this is alleviated upon senescence entry. Notably, SICC formation is reminiscent of "phase separation" (Hnisz et al., 2017), but proved reversible upon reintroduction of HMGB2, which should perhaps be expected for an early event on the path to senescence. Another notable feature is that HMGB1/B2 have been detected bound to mitotic chromatin (Pallier et al., 2003) in a manner similar to another HMGB box factor, Sox2 (Teves et al., 2016). This opens up the possibility of mitotic bookmarking by HMGB2, thus connecting proliferative capacity to topological demarcation and looping. Although further work is needed, such bookmarking could explain the inability of lung adenocarcinoma cells to propagate in the persistent absence of HMGB2. We propose that deregulation of higher-order chromatin organization via the nuclear depletion of HMGB2 constitutes a deterministic primer for the ensuing senescent program across cell types, and HMGB2 itself acts as a rheostat of topological insulation, the depletion of which reversibly affects global transcription competency and heterochromatin organization.

STAR★METHODS

Detailed methods are provided in the online version of this paper and include the following:

- KEY RESOURCES TABLE
- CONTACT FOR REAGENT AND RESOURCE SHARING
- EXPERIMENTAL MODEL AND SUBJECT DETAILS
  - Primary human cell lines and senescence markers
- METHOD DETAILS
  - Immunofluorescence and image analysis
  - Genome-wide chromosome conformation capture (Hi-C) and analysis
  - RNA isolation, sequencing, and analysis
  - 3D-DNA FISH and high-throughput imaging
  - Molecular dynamics simulations
  - ChIP-seq and analysis
  - CTCF-HiChIP and analysis
  - Protein extraction and western blotting
  - EdU and EU labeling of nucleic acids
  - Single-cell mRNA sequencing and analysis
  - siRNA-mediated *HMGB2* knock-down
  - SICC rescue experiments
- QUANTIFICATION AND STATISTICAL ANALYSIS
  - Image analyses
  - Statistical tests
- DATA AND SOFTWARE AVAILABILITY

SUPPLEMENTAL INFORMATION

Supplemental Information includes ten figures and four tables and can be found with this article online at https://doi.org/10.1016/j.molcel.2018.03.030.

ACKNOWLEDGMENTS

We would like to thank George Garinis, Leo Kurian, and Alvaro Rada-Iglesias for discussions, and the CECAD facility for help with gSTED imaging. This work was supported by IZKF funding (I.G.C.); the Else Kröner Fresenius Stiftung (2014-A193; W.W. and A.P.); a DFG grant (PA2456/5-1; K.R. and A.P.); and the CMMC (2635/7708/01), a UoC Advanced Postdoc Grant (3622/8011/11), and the Fritz Thyssen Stiftung (3D-DM1; A.P.). The Opera Phenix High Content Screening System is supported by the DFG Major Research Instrumentation Program (INST 247/845-1 FUGG; V.R.).

AUTHOR CONTRIBUTIONS

A.Z., M.N., and A.P. conceived research; A.Z., K.S., T.G., and L.B. performed experiments; J.-P.M. and K.R. performed scRNA-seq; H.G., O.D., and V.R. generated 3D DNA-FISH data; C.B., J.A., and P.N. assisted with NGS sequencing; M.N. and N.J. analyzed NGS data; M.K. and R.T.U. provided adenocarcinoma data; J.F. and W.W. provided methylation data and MSCs; E.G.G. and I.G.C. provided ChIP-seq motif analysis; C.A.B. and D.M. performed simulations with input from A.P.; and A.Z., M.N., K.S., and A.P. wrote the manuscript with input from all co-authors.

DECLARATION OF INTERESTS

W.W. is a cofounder of Cygenia GmbH.

Received: September 14, 2017
Revised: February 19, 2018
Accepted: March 25, 2018
Published: April 26, 2018

REFERENCES

Abraham, A.B., Bronstein, R., Reddy, A.S., Maletic-Savatic, M., Aguirre, A., and Tsirka, S.E. (2013). Aberrant neural stem cell proliferation and increased adult neurogenesis in mice lacking chromatin protein HMGB2. PLoS ONE *8*, e84838.

Acosta, J.C., Banito, A., Wuestefeld, T., Georgilis, A., Janich, P., Morton, J.P., Athineos, D., Kang, T.W., Lasitschka, F., Andrulis, M., et al. (2013). A complex secretory program orchestrated by the inflammasome controls paracrine senescence. Nat. Cell Biol. *15*, 978–990.

Aird, K.M., Iwasaki, O., Kossenkov, A.V., Tanizawa, H., Fatkhutdinov, N., Bitler, B.G., Le, L., Alicea, G., Yang, T.L., Johnson, F.B., et al. (2016). HMGB2 orchestrates the chromatin landscape of senescence-associated secretory phenotype gene loci. J. Cell Biol. *215*, 325–334.

Belton, J.M., McCord, R.P., Gibcus, J.H., Naumova, N., Zhan, Y., and Dekker, J. (2012). Hi-C: a comprehensive technique to capture the conformation of genomes. Methods *58*, 268–276.

Bonaldi, T., Längst, G., Strohner, R., Becker, P.B., and Bianchi, M.E. (2002). The DNA chaperone HMGB1 facilitates ACF/CHRAC-dependent nucleosome sliding. EMBO J. *21*, 6865–6873.

Brackley, C.A., Johnson, J., Kelly, S., Cook, P.R., and Marenduzzo, D. (2016a). Simulated binding of transcription factors to active and inactive regions folds human chromosomes into loops, rosettes and topological domains. Nucleic Acids Res. *44*, 3503–3512.

Brackley, C.A., Brown, J.M., Waithe, D., Babbs, C., Davies, J., Hughes, J.R., Buckle, V.J., and Marenduzzo, D. (2016b). Predicting the three-dimensional folding of cis-regulatory regions in mammalian genomes using bioinformatic data and polymer models. Genome Biol. *17*, 59.

Chandra, T., Ewels, P.A., Schoenfelder, S., Furlan-Magaril, M., Wingett, S.W., Kirschner, K., Thuret, J.Y., Andrews, S., Fraser, P., and Reik, W. (2015). Global reorganization of the nuclear landscape in senescent cells. Cell Rep. *10*, 471–483.

Criscione, S.W., De Cecco, M., Siranosian, B., Zhang, Y., Kreiling, J.A., Sedivy, J.M., and Neretti, N. (2016). Reorganization of chromosome architecture in replicative cellular senescence. Sci. Adv. *2*, e1500882.

Cruickshanks, H.A., McBryan, T., Nelson, D.M., Vanderkraats, N.D., Shah, P.P., van Tuyn, J., Singh Rai, T., Brock, C., Donahue, G., Dunican, D.S., et al. (2013). Senescent cells harbour features of the cancer epigenome. Nat. Cell Biol. *15*, 1495–1506.

Davalos, A.R., Kawahara, M., Malhotra, G.K., Schaum, N., Huang, J., Ved, U., Beausejour, C.M., Coppe, J.P., Rodier, F., and Campisi, J. (2013). p53-dependent release of Alarmin HMGB1 is a central mediator of senescent phenotypes. J. Cell Biol. *201*, 613–629.

De Cecco, M., Criscione, S.W., Peckham, E.J., Hillenmeyer, S., Hamm, E.A., Manivannan, J., Peterson, A.L., Kreiling, J.A., Neretti, N., and Sedivy, J.M. (2013). Genomes of replicatively senescent cells undergo global epigenetic changes leading to gene silencing and activation of transposable elements. Aging Cell *12*, 247–256.

de Keizer, P.L. (2017). The fountain of youth by targeting senescent cells? Trends Mol. Med. *23*, 6–17.

Dixon, J.R., Selvaraj, S., Yue, F., Kim, A., Li, Y., Shen, Y., Hu, M., Liu, J.S., and Ren, B. (2012). Topological domains in mammalian genomes identified by analysis of chromatin interactions. Nature *485*, 376–380.

ENCODE Project Consortium (2012). An integrated encyclopedia of DNA elements in the human genome. Nature *489*, 57–74.

Franzen, J., Zirkel, A., Blake, J., Rath, B., Benes, V., Papantonis, A., and Wagner, W. (2017). Senescence-associated DNA methylation is stochastically acquired in subpopulations of mesenchymal stem cells. Aging Cell *16*, 183–191.

Gusmao, E.G., Dieterich, C., Zenke, M., and Costa, I.G. (2014). Detection of active transcription factor binding sites with the combination of DNase hypersensitivity and histone modifications. Bioinformatics *30*, 3143–3151.

Haghverdi, L., Büttner, M., Wolf, F.A., Buettner, F., and Theis, F.J. (2016). Diffusion pseudotime robustly reconstructs lineage branching. Nat. Methods *13*, 845–848.

Hayflick, L. (1965). The limited in vitro lifetime of human diploid cell strains. Exp. Cell Res. *37*, 614–636.

Herbig, U., Jobling, W.A., Chen, B.P., Chen, D.J., and Sedivy, J.M. (2004). Telomere shortening triggers senescence of human cells through a pathway involving ATM, p53, and p21(CIP1), but not p16(INK4a). Mol. Cell *14*, 501–513.

Hernandez-Segura, A., de Jong, T.V., Melov, S., Guryev, V., Campisi, J., and Demaria, M. (2017). Unmasking transcriptional heterogeneity in senescent cells. Curr. Biol. *27*, 2652–2660.e4.

Hnisz, D., Shrinivas, K., Young, R.A., Chakraborty, A.K., and Sharp, P.A. (2017). A phase separation model for transcriptional control. Cell *169*, 13–23.

Hoare, M., and Narita, M. (2017). NOTCH and the 2 SASPs of senescence. Cell Cycle *16*, 239–240.

Kotsantis, P., Silva, L.M., Irmscher, S., Jones, R.M., Folkes, L., Gromak, N., and Petermann, E. (2016). Increased global transcription activity as a mechanism of replication stress in cancer. Nat. Commun. *7*, 13087.

Kruse, K., Hug, C.B., Hernández-Rodríguez, B., and Vaquerizas, J.M. (2016). TADtool: visual parameter identification for TAD-calling algorithms. Bioinformatics *32*, 3190–3192.

Lareau, C.A., and Aryee, M.J. (2018). hichipper: a preprocessing pipeline for calling DNA loops from HiChIP data. Nat. Methods *15*, 155–156.

Laurent, B., Randrianarison-Huetz, V., Maréchal, V., Mayeux, P., Dusanter-Fourt, I., and Duménil, D. (2010). High-mobility group protein HMGB2 regulates human erythroid differentiation through trans-activation of GFI1B transcription. Blood *115*, 687–695.

Lee, D., Kwon, J.H., Kim, E.H., Kim, E.S., and Choi, K.Y. (2010). HMGB2 stabilizes p53 by interfering with E6/E6AP-mediated p53 degradation in human papillomavirus-positive HeLa cells. Cancer Lett. *292*, 125–132.

Li, H., and Durbin, R. (2010). Fast and accurate long-read alignment with Burrows-Wheeler transform. Bioinformatics *26*, 589–595.

Little, A.J., Corbett, E., Ortega, F., and Schatz, D.G. (2013). Cooperative recruitment of HMGB1 during V(D)J recombination through interactions with RAG1 and DNA. Nucleic Acids Res. *41*, 3289–3301.

Ly, D.H., Lockhart, D.J., Lerner, R.A., and Schultz, P.G. (2000). Mitotic misregulation and human aging. Science *287*, 2486–2492.

Madsen, J.G., Schmidt, S.F., Larsen, B.D., Loft, A., Nielsen, R., and Mandrup, S. (2015). iRNA-seq: computational method for genome-wide assessment of acute transcriptional regulation from total RNA-seq data. Nucleic Acids Res. *43*, e40.

Marx, A., Backes, C., Meese, E., Lenhof, H.P., and Keller, A. (2016). EDISON-WMW: exact dynamic programing solution of the Wilcoxon-Mann-Whitney test. Genomics Proteomics Bioinformatics *14*, 55–61.

Melnik, S., Caudron-Herger, M., Brant, L., Carr, I.M., Rippe, K., Cook, P.R., and Papantonis, A. (2016). Isolation of the protein and RNA content of active sites of transcription from mammalian cells. Nat. Protoc. *11*, 553–565.

Mumbach, M.R., Rubin, A.J., Flynn, R.A., Dai, C., Khavari, P.A., Greenleaf, W.J., and Chang, H.Y. (2016). HiChIP: efficient and sensitive analysis of protein-directed genome architecture. Nat. Methods *13*, 919–922.

Narita, M., Narita, M., Krizhanovsky, V., Nuñez, S., Chicas, A., Hearn, S.A., Myers, M.P., and Lowe, S.W. (2006). A novel role for high-mobility group a proteins in cellular senescence and heterochromatin formation. Cell *126*, 503–514.

Naumova, N., Imakaev, M., Fudenberg, G., Zhan, Y., Lajoie, B.R., Mirny, L.A., and Dekker, J. (2013). Organization of the mitotic chromosome. Science *342*, 948–953.

Neyret-Kahn, H., Benhamed, M., Ye, T., Le Gras, S., Cossec, J.C., Lapaquette, P., Bischof, O., Ouspenskaia, M., Dasso, M., Seeler, J., et al. (2013). Sumoylation at chromatin governs coordinated repression of a transcriptional program essential for cell growth and proliferation. Genome Res. *23*, 1563–1579.

Orlando, D.A., Chen, M.W., Brown, V.E., Solanki, S., Choi, Y.J., Olson, E.R., Fritz, C.C., Bradner, J.E., and Guenther, M.G. (2014). Quantitative ChIP-seq normalization reveals global modulation of the epigenome. Cell Rep. *9*, 1163–1170.

Pallier, C., Scaffidi, P., Chopineau-Proust, S., Agresti, A., Nordmann, P., Bianchi, M.E., and Marechal, V. (2003). Association of chromatin proteins high mobility group box (HMGB) 1 and HMGB2 with mitotic chromosomes. Mol. Biol. Cell *14*, 3414–3426.

Plimpton, S. (1995). Fast parallel algorithms for short-range molecular-dynamics. J. Comp. Physiol. *117*, 1–19.

Polanská, E., Dobšáková, Z., Dvořáčková, M., Fajkus, J., and Štros, M. (2012). HMGB1 gene knockout in mouse embryonic fibroblasts results in reduced telomerase activity and telomere dysfunction. Chromosoma *121*, 419–431.

Rai, T.S., and Adams, P.D. (2013). Lessons from senescence: chromatin maintenance in non-proliferating cells. Biochim. Biophys. Acta *1819*, 322–331.

Rai, T.S., Cole, J.J., Nelson, D.M., Dikovskaya, D., Faller, W.J., Vizioli, M.G., Hewitt, R.N., Anannya, O., McBryan, T., Manoharan, I., et al. (2014). HIRA orchestrates a dynamic chromatin landscape in senescence and is required for suppression of neoplasia. Genes Dev. *28*, 2712–2725.

Rao, S.S., Huntley, M.H., Durand, N.C., Stamenova, E.K., Bochkov, I.D., Robinson, J.T., Sanborn, A.L., Machol, I., Omer, A.D., Lander, E.S., and Aiden, E.L. (2014). A 3D map of the human genome at kilobase resolution reveals principles of chromatin looping. Cell *159*, 1665–1680.

Rao, J., Pfeiffer, M.J., Frank, S., Adachi, K., Piccini, I., Quaranta, R., Araúzo-Bravo, M., Schwarz, J., Schade, D., Leidel, S., et al. (2016). Stepwise clearance of repressive roadblocks drives cardiac induction in human ESCs. Cell Stem Cell *18*, 341–353.

Redmond, A.M., Byrne, C., Bane, F.T., Brown, G.D., Tibbitts, P., O'Brien, K., Hill, A.D., Carroll, J.S., and Young, L.S. (2015). Genomic interaction between ER and HMGB2 identifies DDX18 as a novel driver of endocrine resistance in breast cancer cells. Oncogene *34*, 3871–3880.

Risso, D., Ngai, J., Speed, T.P., and Dudoit, S. (2014). Normalization of RNA-seq data using factor analysis of control genes or samples. Nat. Biotechnol. *32*, 896–902.

Roukos, V., Pegoraro, G., Voss, T.C., and Misteli, T. (2015). Cell cycle staging of individual cells by fluorescence microscopy. Nat. Protoc. *10*, 334–348.

Rowley, M.J., Nichols, M.H., Lyu, X., Ando-Kuri, M., Rivera, I.S.M., Hermetz, K., Wang, P., Ruan, Y., and Corces, V.G. (2017). Evolutionarily conserved principles predict 3D chromatin organization. Mol. Cell *67*, 837–852.e7.

Sadaie, M., Salama, R., Carroll, T., Tomimatsu, K., Chandra, T., Young, A.R., Narita, M., Pérez-Mancera, P.A., Bennett, D.C., Chong, H., et al. (2013). Redistribution of the Lamin B1 genomic binding profile affects rearrangement of heterochromatic domains and SAHF formation during senescence. Genes Dev. *27*, 1800–1808.

Servant, N., Lajoie, B.R., Nora, E.P., Giorgetti, L., Chen, C.J., Heard, E., Dekker, J., and Barillot, E. (2012). HiTC: exploration of high-throughput 'C' experiments. Bioinformatics *28*, 2843–2844.

Shachar, S., Voss, T.C., Pegoraro, G., Sciascia, N., and Misteli, T. (2015). Identification of gene positioning factors using high-throughput imaging mapping. Cell *162*, 911–923.

Shah, P.P., Donahue, G., Otte, G.L., Capell, B.C., Nelson, D.M., Cao, K., Aggarwala, V., Cruickshanks, H.A., Rai, T.S., McBryan, T., et al. (2013). Lamin B1 depletion in senescent cells triggers large-scale changes in gene expression and the chromatin landscape. Genes Dev. *27*, 1787–1799.

Shen, L., Shao, N., Liu, X., and Nestler, E. (2014). ngs.plot: quick mining and visualization of next-generation sequencing data by integrating genomic databases. BMC Genomics *15*, 284.

Smith, J.R., and Whitney, R.G. (1980). Intraclonal variation in proliferative potential of human diploid fibroblasts: stochastic mechanism for cellular aging. Science *207*, 82–84.

Spitzer, M., Wildenhain, J., Rappsilber, J., and Tyers, M. (2014). BoxPlotR: a web tool for generation of box plots. Nat. Methods *11*, 121–122.

Stros, M. (2010). HMGB proteins: interactions with DNA and chromatin. Biochim. Biophys. Acta *1799*, 101–113.

Swanson, E.C., Manning, B., Zhang, H., and Lawrence, J.B. (2013). Higher-order unfolding of satellite heterochromatin is a consistent and early event in cell senescence. J. Cell Biol. *203*, 929–942.

Taniguchi, N., Caramés, B., Ronfani, L., Ulmer, U., Komiya, S., Bianchi, M.E., and Lotz, M. (2009). Aging-related loss of the chromatin protein HMGB2 in articular cartilage is linked to reduced cellularity and osteoarthritis. Proc. Natl. Acad. Sci. USA *106*, 1181–1186.

Teves, S.S., An, L., Hansen, A.S., Xie, L., Darzacq, X., and Tjian, R. (2016). A dynamic mode of mitotic bookmarking by transcription factors. eLife *5*, e22280.

Tripathi, S., Pohl, M.O., Zhou, Y., Rodriguez-Frandsen, A., Wang, G., Stein, D.A., Moulton, H.M., DeJesus, P., Che, J., Mulder, L.C., et al. (2015). Meta- and orthogonal integration of influenza "OMICs" data defines a role for UBR4 in virus budding. Cell Host Microbe *18*, 723–735.

van Deursen, J.M. (2014). The role of senescent cells in ageing. Nature *509*, 439–446.

Wagle, P., Nikolić, M., and Frommolt, P. (2015). QuickNGS elevates next-generation sequencing data analysis to a new level of automation. BMC Genomics *16*, 487.

Yang, T., Zhang, F., Yardımcı, G.G., Song, F., Hardison, R.C., Noble, W.S., Yue, F., and Li, Q. (2017). HiCRep: assessing the reproducibility of Hi-C data using a stratum-adjusted correlation coefficient. Genome Res. *27*, 1939–1949.

Zhang, R., Poustovoitov, M.V., Ye, X., Santos, H.A., Chen, W., Daganzo, S.M., Erzberger, J.P., Serebriiskii, I.G., Canutescu, A.A., Dunbrack, R.L., et al. (2005). Formation of MacroH2A-containing senescence-associated heterochromatin foci and senescence driven by ASF1a and HIRA. Dev. Cell *8*, 19–30.

Zhang, Y., Liu, T., Meyer, C.A., Eeckhoute, J., Johnson, D.S., Bernstein, B.E., Nusbaum, C., Myers, R.M., Brown, M., Li, W., and Liu, X.S. (2008). Model-based analysis of ChIP-seq (MACS). Genome Biol. *9*, R137.

STAR★METHODS

KEY RESOURCES TABLE

REAGENT or RESOURCE	SOURCE	IDENTIFIER
Antibodies		
Mouse monoclonal anti-HMGB1 (1:1000)	Abcam	ab190377 (1F3)
Rabbit polyclonal anti-HMGB2 (1:1000)	Abcam	ab67282; RRID: AB_1140885
Mouse monoclonal anti-HMGB1/2 (1:1000)	Sigma-Aldrich	12248-3D2 (3D2)
Rabbit polyclonal anti-CTCF (1:500)	Active motif	61311; RRID: AB_2614975
Mouse monoclonal anti-HP1α (1:500)	Active motif	39977 (2HP-1H5); RRID: AB_2614983
Mouse monoclonal anti-H3K9me3 (1:200)	Active motif	39286 (2AG-6F12-H4)
Rabbit polyclonal anti-H3K27me3 (1:1000)	Diagenode	C15410069
Rabbit polyclonal anti-H3K27ac (1:500)	Diagenode	C15410174; RRID: AB_2716835
Mouse monoclonal anti-H4K16ac (1:500)	Active motif	61529 (MABI 0416)
Mouse monoclonal anti-p21 (1:500)	Abcam	ab184640 (GT1032)
Rabbit polyclonal anti-Lamin B1 (1:2000)	Abcam	ab16048; RRID: AB_443298
Rabbit polyclonal anti-Rad21 (1:1000)	Abcam	ab992; RRID: AB_2176601
Goat polyclonal anti-SMC1A (1:500)	Bethyl	A303-834A; RRID: AB_2620185
Mouse monoclonal anti-β-Tubulin (1:1000)	Sigma-Aldrich	T0198 (D66); RRID: AB_477556
Critical Commercial Assays		
MTT proliferation assays	Invitrogen	M6494
Senescence CpG methylation	Cygenia GmbH	Custom service
Click-IT RNA Alexa 488 fluor kit	Thermo Fisher	C10329
Deposited Data		
Raw and analyzed sequencing data	This paper	GEO: GSE98448
Experimental Models: Cell Lines		
HUVEC (single donor)	Lonza	N/A
IMR90	Coriell	I-10 and I-79
MSC	Franzen et al., 2017	N/A
Oligonucleotides		
ChIP-qPCR primers	This paper	see Table S4
Accel-siRNA pool targeting *HMGB2*	Dharmacon	E-011689-00-0010
Accel-siRNA control kit - red	Dharmacon	K-005000-R1-01
Recombinant DNA		
HMGB2-GFP fusion construct	This paper	N/A
piggybac GFP-fusion vector	Rao et al., 2016	KA0717
piggybac transactivator vector	Rao et al., 2016	KA0637
Transposase-encoding vector	SBI Biosciences	PB200PA-1
Software and Algorithms		
NuclearParticleDetector2D (from MiToBo)	N/A	http://mitobo.informatik.uni-halle.de/index.php/Main_Page
Burrows-Wheeler Aligner	Li and Durbin, 2010	http://bio-bwa.sourceforge.net/
Picard tools	N/A	http://broadinstitute.github.io/picard/
HiTC	Servant et al., 2012	https://bioconductor.org/packages/release/bioc/html/HiTC.html
MACS2	Zhang et al., 2008	https://github.com/taoliu/MACS
hichipper	Lareau and Aryee, 2018	https://github.com/aryeelab/hichipper
QuickNGS	Wagle et al., 2015	https://sourceforge.net/projects/quickngs
RUVseq	Risso et al., 2014	https://bioconductor.org/packages/release/bioc/html/RUVSeq.html
ngs.plot	Shen et al., 2014	https://github.com/shenlab-sinai/ngsplot

(*Continued on next page*)

Continued

REAGENT or RESOURCE	SOURCE	IDENTIFIER
iRNaseq	Madsen et al., 2015	http://bioinformatik.sdu.dk/solexa/webshare/iRNA/iRNA-v1.1-script.tar.gz
BoxPlotR	Spitzer et al., 2014	http://shiny.chemgrid.org/boxplotr/
Metascape	Tripathi et al., 2015	http://metascape.org/gp/index.html
TADtool	Kruse et al., 2016	https://github.com/vaquerizaslab/tadtool
Harmony (v. 4.4)	PerkinElmer	http://www.perkinelmer.com/product/harmony-4-6-office-hh17000001
Graphpad	N/A	https://graphpad.com/
3D Genome Browser	N/A	http://promoter.bx.psu.edu/hi-c/
EDISON-WMW tool	Marx et al., 2016	https://ccb-compute2.cs.uni-saarland.de/wtest/?id%20=%20www/www-ccb/html/wtest

CONTACT FOR REAGENT AND RESOURCE SHARING

Further information and requests for reagents may be directed to and will be fulfilled by the Lead Contact, Argyris Papantonis (argyris.papantonis@uni-koeln.de).

EXPERIMENTAL MODEL AND SUBJECT DETAILS

Primary human cell lines and senescence markers

HUVECs from single, apparently healthy, donors (passage 2; Lonza) were continuously passaged to replicative exhaustion in complete Endopan-2 supplemented with 2% FBS under 5% CO_2. Cells were constantly seeded at ~10,000 cells/cm^2, except late passages that were seeded at ~20,000 cells/cm^2. Single IMR90 isolates (I90-10 and −79, passage 5; Coriell Biorepository) were continuously passaged to replicative exhaustion in MEM (M4655, Sigma-Aldrich) supplemented with non-essential amino acids and 20% FBS under 5% CO_2. Mesenchymal stromal cells (MSCs) were isolated at the Aachen Medical School, and cultured to senescence as previously described (Franzen et al., 2017). Cell proliferation was monitored by MTT assays at different passages. In brief, ~5,000 cells are seeded in 96-well format plates in quadruplicates. On the next day, the medium is replaced with 100 μl fresh medium plus 10 μl of a 12 μM MTT stock solution (Invitrogen), and cells are incubated at 37°C for 4 h. Subsequently, all but 25 μL of the medium is removed from the wells, and formazan dissolved in 50 μL DMSO, mixed thoroughly and incubated at 37°C for 10 min. Samples are then mixed again and absorbance read at 530 nm. Measurements are taken at 24, 48 and 72 h post-seeding, background subtracted, and normalized to the 24 h time point. Senescence-associated β-galactosidase assay (Cell Signaling) was performed according to the manufacturer's instructions to evaluate the fraction of senescent cells at different passages. Finally, DNA methylation at six selected CpG islands (Franzen et al., 2017) was measured by isolating genomic DNA at the different cell states and performing targeted pyrosequencing (Cygenia GmbH).

METHOD DETAILS

Immunofluorescence and image analysis

Cells were grown on coverslips from the stage indicated; they were fixed in 4% PFA/PBS for 15 min at room temperature. After washing once in PBS, cells were permeabilized with 0.5% Triton-X/PBS for 5 min at room temperature. Blocking with 1% BSA/PBS for 1h was followed by incubation with the indicated primary antibodies for 1-2 h. Cells were washed twice with PBS for 5 min before incubating with secondary antibodies for 1 h at room temperature. Nuclei were stained with DAPI (Sigma-Aldrich) for 5 min, washed, and coverslips mounted onto slides in Prolong Gold Antifade (Invitrogen). For image acquisition, a widefield Leica DMI 6000B with a HCX PL APO 63x/1.40 (Oil) objective was used; confocal and super-resolution images were acquired on a Leica TCS SP8 gSTED microscope with a 100x/1.40 (Oil) STED Orange objective. Deconvolution of super-resolution images was performed using the Huygens software from Scientific Volume Imaging. Note that for the immunostainings of pre-extracted nuclei (Figure S9F), cells grown on overspills were incubated in CSK buffer (10 mM HEPES pH 7.9, 300 mM sucrose, 100 mM Nacl, 3 mM $MgCl_2$) for 1 min at room temperature, and then in CSK+0.5% Triton X-100 for 1 min at room temperature before fixation as described above.

Genome-wide chromosome conformation capture (Hi-C) and analysis

For Hi-C studies, 25-35 million proliferating/senescent HUVEC were crosslinked by adding 1% PFA (Electron Microscopy Sciences) for 10 min at room temperature with subsequent quenching (125 mM glycine), and gently scraped off the plates on ice. Then, Hi-C was performed as previously described (Belton et al., 2012) under conditions where nuclei remained largely intact. In brief, cells were lysed (10 mM Tris-HCl pH 8.0, 10 mM NaCl, 0.4% NP40, 1x protease inhibitor cocktail) twice for 20 min on ice, washed with

1x NEBuffer 2 twice, and distributed into 4-5 tubes. Following SDS treatment (0.1%) for 10 min at 65°C and quenching with Triton-X for 15 min at 37°C, chromatin was digested with 600 units of *Hind*III overnight at 37°C under constant agitation. Next day, digestion was extended for another hour with an additional 600 units of *Hind*III for 1-2 hours. DNA overhangs were filled-in using a biotin-dCTP containing mix (1.5μl dATP, 1.5 μl dGTP, 1.5 μl dTTP, 37.7 μl biotin-dCTP, each 10 mM stock; Invitrogen) in the presence of 1.5 μl 50 U/μl Klenow (NEB) for 45min at 37°C, and all enzymes are inactivated by adding 86 μl 10% SDS to all tubes and incubating for 30min at 65°C. Next, each individual mixture was transferred into a 15 mL tube, incubated for 10-20min on ice to quench SDS, and a mixture containing 745 μl of 10% Triton-X, 745 μl 10x ligation buffer (500 mM Tris-HCl pH 7.5, 100 mM $MgCl_2$, 100 mM DTT), 80 μl of a 10 mg/ml BSA stock, 80 μl of 100 mM ATP and 5.96 mL milliQ water is added to each tube, and blunt-end ligation initiated by adding 15 μl of 5 U/μl T4 DNA ligase (Invitrogen) and incubated for 6 hours at 16°C. Crosslinks were then reversed and proteins degraded by adding 35 μl of 15mg/ml proteinase K and incubated overnight at 65°C. Next day, an additional 35 μl of proteinase K was added for 2 hours at 65°C, mixtures were cooled to room temperature, transferred to 50 mL tubes, and DNA was extracted twice with phenol:chloroform (pH 8.0) and ethanol precipitated. The resulting pellets were dissolved in 450 μl 1x TE, transferred to 1.7ml tubes, DNA was re-extracted twice, precipitated, pellets were washed once in 70% ethanol, air-dried, and resuspended in 25 μl 1x TE. Subsequently, three tubes, each with ~5 μg of the Hi-C template, were incubated for 2 h at 12°C in the presence of 1 μl 10 mg/ml BSA, 10 μl 10x NEBuffer 2, 1 μl 10 mM dATP, 1 μl 10 mM dGTP (for *Nco*I samples dCTP was used instead) and 5 units of T4 DNA polymerase (NEB) in a total volume of 100 μl to remove biotin-16-dCTP at non-ligated DNA ends. Reactions were stopped by adding 2 μl of 0.5 M EDTA pH 8.0, and the DNA was subsequently purified by phenol extraction and ethanol precipitation. DNA pellets were resuspended and pooled in a total of 100μl of milliQ water, and residual salts were removed via Amicon 30K columns via three washing steps (1x 200 μl and 2x 100 μl milliQ water). Finally, DNA was sheared to a size of 300-600 bp on a Bioruptor Plus (Diagenode; 2x 10 cycles of 30 s *on* and 30 s *off*, at the highest power setting).

For IMR90 and MSC cells, the procedure was slightly modified to follow the *in situ* Hi-C protocol (Rao et al., 2014). Approx. 20 million cells were lysed twice in 900 μl lysis buffer (10 mM Tris-HCl pH 8.0, 10 mM NaCl, 0.4% NP-40, 1x protease inhibitor cocktail) for 15 min on ice, nuclei were pelleted and washed once in 1x NEBuffer 2, distributed into 4 tubes, resuspended in 200 μl 0.5% SDS/NEBuffer 2, and incubated for 10 min at 62°C. After repelleting, SDS-treated nuclei were resuspended in 150μl 1% Triton-X/NEBuffer 2, and digested overnight using 400 units of *Hind*III at 37°C with constant agitation. Next day, another 400 units of *Hind*III were added for another 1-2 h at 37°C. Following heat inactivation for 20 min at 62°C, nuclei were pelleted by centrifugation and resuspend in 256 μl NEBuffer 2. DNA ends were then biotinylated by adding 50 μl of a biotin-dCTP-Klenow mix (37.5μl of 0.4 mM biotin-dCTP, 1.5μl of 10 mM dTTP, dATP, and dGTP, and 1.5μl of 50 U/μl Klenow) to each tube and incubating for 1 h at 37°C. Subsequently, 900 μl of ligation mix (603 μl H_2O, 240 μl 5x Invitrogen ligation buffer, 30 μl of 10% Triton-X, 12 μl of 10 mg/ml BSA, and 15 μl ligase) was added to each sample, mixed, and incubated for 6 h at 16°C; tubes were inverted frequently. Nuclei were next pelleted and a volume of 900 μl was removed. Following reversal of crosslinking and proteinase K addition, DNA is phenol:chloroform extracted and ethanol precipitated; all subsequent steps were performed as described above.

Hi-C DNA was used as template for adding sequencing linkers via 10 PCR cycles. Then, Hi-C libraries were sequenced to generate at least 400 million paired-end reads (50-75 bp in length) per each donor/condition on a HiSeq4000 platform (Illumina). Raw reads were mapped to the human reference genome (hg19) iteratively (to ensure maximum recovery of uniquely mapped pairs) using BWA (Li and Durbin, 2010), duplicates were removed (http://picard.sourceforge.net/), and the output converted into BEDPE format. Next, custom R scripts were used to bin the genome into non-overlapping bins (typically 10-kbp ones), assign reads to bins, remove read pairs not representing valid interactions, and to normalize read counts to library size. Finally, the HiTC Bioconductor package was used to annotate, correct matrices for biases in genomic features (Servant et al., 2012), and visualize 2D heatmaps at different resolutions. In addition, we applied a composite, uniform, correction to Hi-C maps from senescent HUVEC due to their tetraploidy; the scaling factor was calculated by adjusting for the ratio of 2n versus 4n cells in the two HUVEC populations (as recorded using DNA FISH; Figure S6A), as well as the shift in *cis-/trans*-contact ratio (expecting the tetraploid cells will have a small bias in favor of cis-interactions. The final factors used were 0.961x for D1, and 0.641x for D2, and were applied before data merging. For subtracted Hi-C maps, we determined bins under a particular cutoff (typically 5 rpm) and set them to 0, while all others were set to 1; then, matrices were subtracted to give a binary appreciation of the interaction changes between the different states. For plotting insulation heatmaps, normalized interactions values in the twenty 20-kbp bins around each HMGB1/B2 peak were added up, normalized to the median value in each bin and plotted. Correlations between Hi-C replicates were calculated on a per chromosome basis using HiCRep (Yang et al., 2017) and 40-kbp resolution data. All R scripts used here are available on request, and all HMGB2-HMGB2 loops identified are listed in Table S1. Note that the visualization of high-resolution Hi-C data (from Rao et al., 2014) was via the "3D Genome Browser" interface (http://promoter.bx.psu.edu/hi-c/).

RNA isolation, sequencing, and analysis

Cell of different types/conditions were harvested in Trizol LS (Life Technologies) and total RNA was isolated and DNase I-treated using the Direct-zol RNA miniprep kit (Zymo Research). Following, rRNA-depletion using the RiboZero Gold kit (Illumina), barcoded cDNA libraries were generated using the TruSeq RNA library kit (Illumina) with (IMR90, MSC) or without selection on poly(dT) beads (HUVEC); in addition some IMR90 and MSC libraries were spiked using a synthetic ERCC Spike-In mix (Thermo Fisher Scientific) to facilitate normalization. The resulting libraries were paired-end sequenced to at least 50 million read pairs on a HiSeq4000 platform (Illumina), and raw reads were mapped to the human reference genome (hg19) and analyzed via the QuickNGS pipeline (Wagle et al.,

2015) to obtain read counts. Then, read counts from different single-donors/conditions were normalized using the RUVSeq package (Risso et al., 2014). Please note that, in our hands, normalization using either synthetic spike-in controls or the intrinsic "top quantile" function of the RUVseq package is essentially interchangeable. Finally, for analysis of nascent RNA in IMR90 the "factory RNA-seq" approach was applied on ~5 million proliferating or senescent cells (Melnik et al., 2016), RNA was isolated and sequenced as above, and intronic read counts were obtained and differentially analyzed for the two conditions using the iRNAseq package (Madsen et al., 2015). All box/bean plots were plotted using the BoxPlotR tool online (http://shiny.chemgrid.org/boxplotr/), and GO term/pathway enrichment analyses using Metascape (http://metascape.org/gp/index.html; Tripathi et al., 2015). Differentially-regulated genes per each cell type are listed in Table S2.

3D-DNA FISH and high-throughput imaging

A three color DNA FISH was performed using the BAC probes RP11-347B21, RP11-296G9 and RP11-781M19 (Chori BACPAC) fluorescently labeled with Alexa 488 dUTP, Alexa 568 dUTP and Alexa 647 dUTP, respectively by nick translation. Briefly, HUVEC and IMR90 cells grown and fixed on coverslips were permeabilized in 0.5% saponin /0.5% Triton X-100/PBS for 20 minutes and incubated in 0.1N HCl for 15 minutes. Following a 30-min incubation in 50% formamide/2X SSC, samples were denatured with the labeled BACs at 85°C for 5 min, and hybridized at 37°C overnight. Three washing steps with 1xSSC and 0.1x SSC were performed before mounting of coverslips with Vectashield containing DAPI onto glass slides. Images were acquired with an Opera Phenix High Content Screening System (PerkinElmer), equipped with four laser lines (405 nm, 488 nm, 568 nm, and 640 nm) and two 16-bit CMOS cameras. Images for 3D and radial distances were acquired in confocal mode using a 40X water objective lens (NA 1.1). For each sample, 13 *z*-planes separated by 0.5 μm were obtained for a total number of at least 108 fields, on a minimum of 1500 cells per condition. For cell cycle staging by DAPI content analysis, cells were imaged using a 20X water objective lens (NA 1.0) in wide-field mode. For each sample, 3 *z*-planes separated by 1 μm were obtained for a total number of 72 fields, on a minimum of 3500 cells per condition.

Molecular dynamics simulations

Polymer simulations in Figure S6 were performed according to a predictive scheme developed previously (Brackley et al., 2016a, 2016b). First, the target region (chr12: 60,000,000-75,000,000; hg19) was divided into 3-kbp windows, each represented by a polymer "bead". Protein complexes are also represented by simple spheres, which interact attractively with specific beads on the polymer. These are determined using IMR90 ChIP-seq data for H3K4me3, H3K36me3, H3K27me3, and H3K9me3 (ENCODE Project Consortium, 2012). We accordingly specified three types of changing bridging proteins and polymer beads. The first type of protein, denoted "active", interacts with polymer beads marked by H3K4me1/3 and H3K36me3 (binding strongly to the enhancer-/promoter-associated marks, and weakly to the H3K36me3 regions); the second type, denoted "repressed", interacts with beads marked by H3K27me3; the third type, denoted "heterochromatin", interacts with beads marked by H3K9me3. Since polymer beads cover 3-kbp, it was possible for a bead to cover regions in different states, and so interact with more than one type of protein; beads not carrying any mark do not interact attractively with any bridging proteins. The dynamics of the diffusing polymer and of the protein complexes are simulated using LAMMPS (Plimpton, 1995) in "Langevin Dynamics" mode; the position of each bead is determined by an equation that describes the potential for interactions between all elements in the system. These potentials include: spring bonds between adjacent beads along the polymer (finite extensible non-linear elastic bonds), angle interactions between triplets of adjacent polymer beads (giving the polymer bending rigidity), steric interactions between all beads to prevent them from overlapping (Weeks-Chandler-Anderson potential), and attractive interactions between protein spheres and polymer beads (shifted truncated Lennard-Jones potential). We performed 48 independent simulations of this 5000-bead polymer with 167 active, 109 H3K27me3-binding, and 165 H3K9me3-binding proteins (these protein numbers were chosen such that the ratio of binding sites to proteins is as previously found to give an optimal prediction of Hi-C data; Brackley et al., 2016b). The system extends 120-bead diameters (σ), the persistence length of the polymer is 4-σ, and we use interaction energies of 5.5 *kBT* and 2 *kBT* for the strong and weak Lennard-Jones interactions, respectively (with a cut-off of 1.8-σ). Each 3-kbp polymer bead has a 30-nm diameter, and each simulation is run for the equivalent of 76 sec. These simulations modelled proliferating cells; to model senescent cells a further set of 48 simulations were performed where we increased the number of H3K9me3-binding proteins by 30% to 220.

For the CTCF clustering simulations in Figure 7, in addition to protein bridges, we also included additional spring interactions between pairs of CTCF sites such that permanent loops form. We used HUVEC ChIP-seq data for H3K4me3, H3K36me3, H3K27me3, and H3K9me3 (ENCODE Project Consortium, 2012) as above to label beads as binding for "active", "repressed" or "heterochromatin" proteins. In each of 48 independent simulations, pairs of convergent CTCF sites are stochastically chosen to form loops depending on the ChIP-seq signal strength in HUVEC data – in this way, a different set of convergent CTCF sites could be looped in each simulation, allowing for cell-to-cell variation. Operating on the hypothesis that CTCF looping is disrupted by the high mobility group proteins, in the case of proliferating cells we switched off any CTCF loops which enclosed HMBG2 binding sites or for which an HMGB2 sites was adjacent to the CTCF site; additionally we switched off protein-bridge binding to beads adjacent to all HMGB2 and CTCF sites. As before the number of heterochromatin binding bridges was 30% higher in the senescent cell simulations. Another possible mechanism for CTCF clustering in senescence is that in these cells there are multimeric interactions between CTCFs (i.e., more than pairwise binding, either directly between CTCF proteins or mediated by another protein); to model this scenario we perform a set of simulations as above, but which also include a direct attractive interaction between all CTCF sites (i.e., fixed-spring interactions between convergent pairs, plus short range attraction between all CTCFs; models "I" and "II" in Figure 7).

ChIP-seq and analysis

For each batch of ChIP experiments approx. 25 million cells, cultured to > 80% confluence in 15-cm dishes, were crosslinked in 15 mM EGS/PBS (ethylene glycol bis(succinimidyl succinate); Thermo) for 20 min at room temperature, followed by fixation for 40 min at 4°C in 1% PFA. From this point onward, cells were processed via the ChIP-IT High Sensitivity kit (Active motif) as per manufacturer's instructions. Chromatin was sheared to 200-500 bp fragments on a Bioruptor Plus (Diagenode; 2x 9 cycles of 30 s *on* and 30 s *off*, at the highest power setting), and immuno-precipitation was carried out by adding 4 μg of the appropriate antiserum (HMGB1: PCRP-HMGB1-4F10 s, DSHB; HMGB2: ab 67282, Abcam; CTCF: 61311, Active motif) to approx. 30 μg of chromatin and incubating on a rotator overnight at 4°C in the presence of protease inhibitors. Following addition of protein A/G agarose beads and washing, DNA was purified using the ChIP DNA Clean & Concentrator kit (Zymo Research) and used in qPCR or next-generation sequencing on a HiSeq4000 platform (Illumina). Where ChIP-seq was performed, at least 35 million reads were obtained and the respective "input" sample was also sequenced. Raw sequencing reads (typically 100 bp-long) were mapped to the reference human genome (hg19) using BWA (Li and Durbin, 2010), and the resulting .BAM files were processed via the MACS2 software (Zhang et al., 2008) to identify signal enrichment over input. Thresholded HMGB1/B2 ChIP-seq peaks per each cell type are listed in Table S1, and oligonucleotides used as primers in ChIP-qPCR listed in Table S4. The .BAM files were also used in ngs.plot (Shen et al., 2014) for plotting ChIP-seq coverage over particular genomic positions for different conditions/cell types. Finally, transcription factor recognition motif enrichments within DHS footprints under HMGB1/B2 ChIP-seq peaks were calculated using the Regulatory Genomics Toolbox (Gusmao et al., 2014). Note that for the H3K27ac/me3 ChIP-seq, crosslinking was with 1% PFA for 10 min at room temperature, rabbit polyclonal antisera were used (H3K27me3: C15410069, H3K27ac: C15410174; Diagenode), and preparations were spiked with chromatin prepared from Drosophila S2 cells as described (Orlando et al., 2014).

CTCF-HiChIP and analysis

For HiChIP (Mumbach et al., 2016) ~30 million proliferating or senescent IMR90 and HUVEC were crosslinked in 1% PFA for 10 min at room temperature with subsequent quenching (125 mM glycine), and gently scraped off the plates on ice. Then, the *in situ* Hi-C protocol described above was applied until the ligation step, and followed by CTCF-bound chromatin immunoprecipitation. Briefly, cells were lysed twice (10 mM Tris-HCl pH 8.0, 10 mM NaCl, 0.4% NP-40, 1x protease inhibitor cocktail) for 15 min on ice, nuclei were pelleted and washed once in 1x NEBuffer 2, distributed into 3 tubes, treated with SDS, and incubated for 10 min at 62°C. Chromatin was digested using *Hind*III (for IMR90) or *Nco*I (for HUVEC) at 37°C. Following heat inactivation, DNA ends were biotinylated by a biotin-dCTP-Klenow mix and incubated for 1 h at 37°C. Subsequently, ligation was performed for 6 h at 16°C, during which tubes were frequently inverted. Nuclei were next pelleted, and 260 μL of shearing buffer (0,1% SDS, 1 mM EDTA, 10 mM Tris-HCl pH 8.0) was used to resuspend the pellet. Sonication was performed using a Bioruptor (Diagenode; 2x 6 cycles of 30 s *on*/30 s *off*, at a low power setting). Immunoprecipitation was carried out by adding 4 μg of the appropriate antiserum (α-CTCF; 61311, Active motif) to approximately 30 μg of biotinylated chromatin before incubating on a rotating platform overnight at 4°C, in the presence of protease inhibitors. Following addition of protein-G magnetic beads (Active motif), DNA was purified using the Chip DNA Clean concentrator kit (Zymo Research). HiChIP DNA was used as template for adding Illumina sequencing linkers via 12 PCR cycles, and libraries were sequenced to generate > 150 million paired-end reads (75-100 bp in length) per condition on a HiSeq4000 platform (Illumina). Raw reads were processed and loops identified using "hichipper" (Lareau and Aryee, 2018).

Protein extraction and western blotting

For assessing protein abundance at the different cell states, approx. 4×10^6 cells were gently scraped off 15-cm dishes, and pelleted for 5 min at 600 x *g*. The supernatant was discarded, and the pellet resuspended in 100 μL of ice-cold RIPA lysis buffer (20 mM Tris-HCl pH 7.5, 150 mM NaCl, 1 mM EDTA pH 8.0, 1 mM EGTA pH 8.0, 1% NP-40, 1% sodium deoxycholate) containing 1x protease inhibitor cocktail (Roche), incubated for 20 min on ice, and centrifuged for 15 min at > 20,000 x *g* to pellet cell debris and collect the supernatant. The concentration of the nuclear extracts was determined using the Pierce BCA Protein Assay Kit (Thermo Fisher Scientific), before extracts were aliquoted and stored at −70°C to be used for western blotting. Resolved proteins were detected using the antisera and dilutions listed in the Key Resources Table.

EdU and EU labeling of nucleic acids

Nascent DNA synthesis was monitored by EdU incorporation and subsequent labeling with the Click-iT chemistry (Click-iT EdU Imaging Kit; Invitrogen). In brief, cells were incubated in 10 μM EdU for 7 h, fixed using 3.7% PFA/PBS for 15 min at room temperature, permeabilized, and labeled as per manufacturer's instructions. Similarly, nascent RNA synthesis was monitored by incorporating EU in transcripts by incubating cells in 1 mM of 5-ethynyl uridine for exactly 5 min at 37°C. Cells were then fixed, permeabilized, and labeled via Click-iT chemistry as above. Before imaging on a widefield Leica microscope as described above, cells were also immunostained for HMGB2, stained with DAPI, and mounted onto glass slides.

Single-cell mRNA sequencing and analysis

Freshly-frozen early- (p. 4) and late-passage HUVEC (p. 16) were thawed, washed once in warm PBS, and subjected immediately to encapsulation in oil droplets. Each droplet contained beads carrying barcoded oligos for cDNA synthesis that allow both cell barcoding and unique transcript identification on a Chromium 10X Genomics platform as per manufacturer's instructions. This way 8,323

early- and 5,269 late-passage cells were processed (with a 0.8% chance of capturing a cell duplet). Samples from each condition were pooled and sequenced separately in two HiSeq2500 lanes each (Illumina) yielding ~30,000 reads per early- and ~47,000 reads per late-passage cell. This accounts for a > 50% sequencing saturation, and returned > 2,500 and > 3,000 robustly captured transcripts for early- and late-passage cells, respectively. Raw sequencing data were processed and visualized using default settings in the Cell Ranger suite provided by the manufacturer.

siRNA-mediated *HMGB2* knock-down

HUVEC or IMR90 were seeded at 20,000 cells/cm^2 the day before transfection. An Accell-siRNA pool (Dharmacon) against *HMGB2*, plus a non-targeting control (NTC; fluorescencently-tagged to allow transfection efficiency to be monitored for each experiment), were added to the cells at a final concentration of 1 μM. Knock-down efficiency and its downstream effects were evaluated at 72 h after transfection using RT-qPCR and/or immunofluorescence assays. For HUVEC Hi-C, cells were seeded the same way but in 2x15cm plates per condition. The cells were crosslinked at 72h post transfection and processed as described for IMR90 and MSC Hi-C. Due to the lower cell number (~5 million cells) permeabilized nuclei were kept in a single tube for downstream processes.

SICC rescue experiments

Doxicycline-inducible overexpression IMR90 cells were generated using PiggyBac transposition. The HMGB2 ORF was TOPO-cloned from cDNA (Invitrogen). Following validation by Sanger sequencing, it was subcloned into the DOX-inducible KA0717 expression vector to generate an HMGB2-GFP fusion. The construct was co-transfected into IMR90 together with transactivator and transposase-encoding vectors (KA0637 and SBI Biosciences #PB200PA-1, respectively) at a DNA mass ratio of 10:1:3 using Fugene HD (PRomega) as per manufacturer's instructions. Stable, transgene-positive, proliferating IMR90 were selected using 250 μg/ml G418 (Sigma Aldrich), and driven into replicative senescence. HMGB2-GFP expression was induced using doxycycline for > 6 h, and IMR90 carrying the empty GFP vector served as a control (for more details see Rao et al., 2016).

QUANTIFICATION AND STATISTICAL ANALYSIS

Image analyses

For immunofluorescence image analysis, the NuclearParticleDetector2D of the "MiToBo" software (from version 1.4.3; available at http://mitobo.informatik.uni-halle.de/index.php/Main_Page) was used. Measurements of nuclear immunofluorescence signal were automatically generated using a mask drawn on DAPI staining to define nuclear bounds. Background subtractions were then used to precisely determine the mean intensity per area of each immunodetected protein. All primary antibodies used here are listed in the Key Resources Table. For STED microscopy only, the 2C Pack STED 775 IR-R- (1:2000; 2-0032-052-6, Abberior) secondary antibodies were used.

For 3D-DNA FISH, image analysis was performed using the Harmony software (version 4.4, PerkinElmer) and custom-made scripts. Segmentation of nuclei was performed via *algorithm B* in maximum-projection images using the DAPI channel. Any cell in the periphery of the image was excluded from further analysis. In each individual nucleus, FISH spots were identified in all three channels using the spot detection *algorithm C*. Distances between all different spots of all different channels were calculated in 2D using custom-made building blocks, while the *z*-plane having the maximum pixel intensity of each spot was identified. Single cell information was then exported as text files and custom R scripts were used to calculate Euclidean distances between the different spots in 3D. In order to only select intrachromosomal distances between the three probes, the minimum distance of each spot (each allele) to other fluorescently labeled alleles was identified and plotted. For data analysis, only cells with equal spot number in all three channels were selected, and at least 1000 cells per condition were analyzed. Distances between spot pairs were plotted as boxplots with 5%–95% whiskers in GraphPad and significances determined by a Mann-Whitney U test. For determination of radial distances of each spot to the nuclear center and border, custom scripts were built based on previous analyses (Shachar et al., 2015). DNA content analysis was performed and plotted as previously described (Roukos et al., 2015).

Statistical tests

P values associated with Student's t tests and Fischer's exact tests were calculated using GraphPad (https://graphpad.com/), those associated with the Wilcoxon-Mann-Whitney test using the EDISON-WMW tool (Marx et al., 2016), while Pearson's correlation coefficients (ρ) using the function embedded in MS Excel (Microsoft). Unless otherwise stated, P values < 0.01 were deemed significant.

DATA AND SOFTWARE AVAILABILITY

The sequencing data generated in this study have been deposited in the NCBI Gene Expression Omnibus (GEO) repository under the accession number GEO: GSE98448.